Critical Review

The Nanoscale Basis of CO2 Trapping for Geologic Storage

Ian C. Bourg, Lauren E. Beckingham, and Donald J. DePaolo

1   # The Nanoscale Basis of CO_2 Trapping for Geologic

2   # Storage

3   *Ian C. Bourg*[1,2], Lauren E. Beckingham[2], and Donald J. DePaolo[2]*

4   [1]Department of Civil and Environmental Engineering and Princeton Environmental Institute,

5   Princeton University, E-208 E-Quad, Princeton, NJ 08544, United States

6   [2]Earth Sciences Division, Lawrence Berkeley National Laboratory, 1 Cyclotron Road, Berkeley,

7   CA 94720, United States

8   KEYWORDS. Carbon Capture and Storage, Geologic Carbon Sequestration, CO2,

9   Nanogeoscience, Shale, Permeability, Multiphase Flow.

10   AUTHOR INFORMATION

11   **Corresponding Author**

12   * Phone: 1-609-258-4541; e-mail: bourg@princeton.edu.

13   **Author Contributions**

14   The manuscript was written through contributions of all authors. All authors have given approval

15   to the final version of the manuscript.

16   **Notes**

17   The authors declare no competing financial interest.

18   ABSTRACT: Carbon capture and storage (CCS) is likely to be a critical technology to achieve

19   large reductions in global carbon emissions over the next century. Research on the subsurface

20   storage of CO_2 is aimed at reducing uncertainties in the efficacy of CO_2 storage in sedimentary

21   rock formations. Three key parameters that have a nanoscale basis and that contribute

22   uncertainty to predictions of CO_2 trapping are the vertical permeability k_v of seals, the residual

23   CO_2 saturation $S_{g,r}$ in reservoir rocks, and the reactive surface area a_r of silicate minerals. This

24   review summarizes recent progress and identifies outstanding research needs in these areas.

25   Available data suggest that the permeability of shale and mudstone seals is heavily dependent on

26   clay fraction and can be extremely low even in the presence of fractures. Investigations of

27   residual CO_2 trapping indicate that CO_2-induced alteration in the wettability of mineral surfaces

28   may significantly influence $S_{g,r}$. Ultimately, the rate and extent of CO_2 conversion to mineral

29   phases are uncertain due to a poor understanding of the kinetics of slow reactions between

30   minerals and fluids. Rapidly improving characterization techniques using X-rays and neutrons,

31   and computing capability for simulating chemical interactions, provide promise for important

32   advances.

33

34   INTRODUCTION

35   Carbon capture and storage (CCS)—the capture of CO_2 from stationary industrial sources,

36   such as power plants, and its long-term storage in geologic reservoirs—is an emerging

37   technology that could contribute up to 55% of global CO_2 abatement efforts over the coming

38   century.[1–7] The overall cost of CCS derives primarily from the cost of separating CO_2 from other

39   gases and is expected to decrease substantially within a decade through new CO_2 capture

40   technologies that already exist at the bench scale.[6,8,9] The storage component of CCS, known as

41   geologic carbon sequestration (GCS), is conceptually straightforward (Fig. 1), relatively

42   inexpensive (< \$12 per ton of CO_2 emissions avoided);[3,4,8-10] and already implemented at a

43   worldwide level of ~16 Mt CO_2 yr^{-1} at industrial and pilot sites in North America, Europe, Asia,

44   Algeria, and Australia.[7,11-17] Technologies for CO_2 transport and geologic injection have been

45   routinely used since the 1970s for CO_2-enhanced oil recovery (CO_2 EOR), a technology

46   currently applied on a scale of ~50 Mt CO_2 yr^{-1} worldwide,[2-4,6,17] and are analogous to the

47   mature technologies applied at hundreds of sites in North America and Europe for natural gas

48   storage and for acid gas and hazardous liquid waste disposal.[1,4] Large CO_2 storage capacities

49   exist worldwide in saline aquifers (1,000 to 10,000 Gt CO_2) and depleted oil and gas reservoirs

50   (675 to 900 Gt CO_2),[3] the storage formations that are the focus of this paper. Additional storage

51   capacity (potentially large, but less well characterized) exists in coal beds,[18] basalt flows,[19]

52   ultramafic aquifers,[20] ocean sediments,[21] and methane clathrate formations.[22]

53   Implementation of CCS as a CO_2 mitigation technology relies heavily on geophysical models

54   to predict the fate of large CO_2 plumes in the subsurface on time scales of weeks to thousands of

55   years.[1,6,11,16,18,23-36] Among the many properties that must be accurately predicted, of foremost

56   importance are predictions of the efficacy of CO_2 trapping mechanisms (Fig. 1). At present,

57   sensitivity analyses and comparisons to data from GCS sites indicate that existing field scale

58   models, while yielding useful qualitative insights, have relatively limited quantitative predictive

59   accuracy in this regard.[11,14-16,18,25,33,37,38] An important limitation to this accuracy, in addition to

60   the well-established challenges associated with upscaling flow and reactivity in heterogeneous

61   porous media, is incomplete knowledge of the parameters and constitutive relations that describe

62   the properties of porous rock-brine-CO_2 systems at the nanoscale, pore-network scale, and core

63   scale.

64
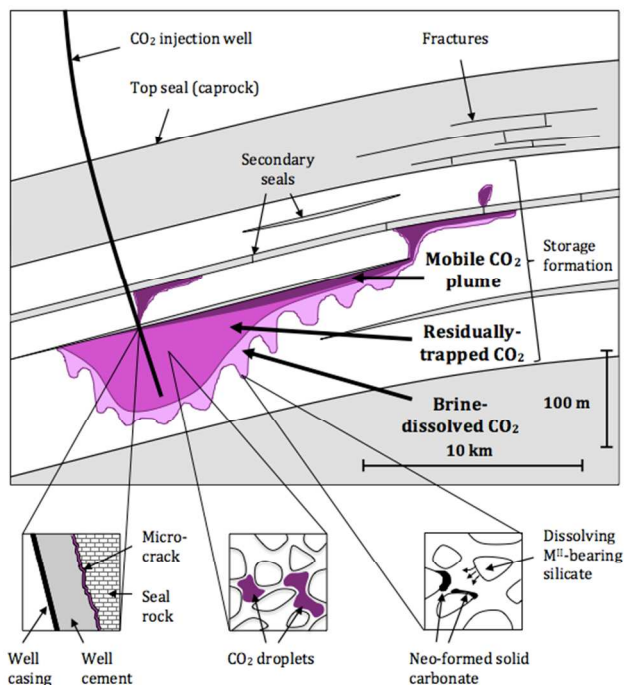
Figure 1. Schematic figure illustrating the distribution of CO_2 near an injection well roughly one decade after the end of injection and the four trapping mechanisms that enable GCS.[1,3–5,7,12,24,26,28,33,39,40] Supercritical CO_2 is injected in previously brine-filled, micrometer scale pore spaces of a highly permeable geologic formation (typically a sandstone) at depths > 800 m, where it is ~30 % less dense than the resident brine. The storage formation is overlain by a thick fine-grained geologic formation, the top seal or caprock, typically a shale or mudstone. The storage formation may contain layers or lenses of fine-grained rock (secondary seals). The vertical migration of the CO_2 plume is retarded or stopped by the seals (stratigraphic trapping). During the migration of the plume, a portion of the CO_2 remains trapped as disconnected droplets at the trailing edge of the plume (residual trapping). On time scales of thousands of years, CO_2 dissolves in the formation water (solubility trapping), reacts with silicate minerals, and precipitates as solid carbonate (mineral trapping). Plume dimensions may reach ~10 km in

77   width and ~100 m in height. The vertical scale is expanded roughly 50 times relative to the

78   horizontal scale.

79

80   In the present paper, we examine three parameters used in field scale GCS models that have a

81   clear nanoscale basis and that contribute significantly to the uncertainty of field scale predictions

82   of CO_2 trapping: the vertical permeability k_v of seals,[18,24,26,30,33,41] the residual CO_2 saturation $S_{g,r}$

83   in reservoir rocks,[14,15,23,24,41] and the reactive surface area a_r of silicate solids.[42–46] For the sake of

84   brevity, we do not address the equally interesting nanoscale basis of geothermal effects,[47]

85   solubility trapping,[48] or the impact of impurities such as SO_2 or H_2S.[49] We also do not discuss

86   processes that are not directly related to CO_2 trapping, such as CO_2 invasion in reservoir

87   rocks,[50,51] CO_2 molecular diffusion in natural gas reservoirs,[52] monitoring,[17] injectivity,[53]

88   colloidal transport,[54] induced seismicity,[39] CO_2-brine-rock equations of state,[55] CO_2 plume shape

89   and velocity,[37] or the potential consequences of CO_2 leakage[56,57] or that do not have a clear

90   nanoscale basis, such as reservoir topography[12,58] and heterogeneity.[59,60] We focus on examining

91   how nanoscale phenomena influence core scale properties associated with CO_2 trapping in rock-

92   brine-CO_2 systems.

93

94   KEY PARAMETERS IN CO_2 TRAPPING PREDICTIONS

95   **Stratigraphic trapping: vertical permeability (k_v) of fine-grained rock formations.** The

96   fluid transport properties of seals (vertical permeability k_v, capillary breakthrough pressure $P_{c,b}$)

97   strongly influence the rate of dissipation of reservoir overpressure, plume shape (hence sweep

98   efficiency), upward plume migration velocity, the rate of CO_2 dissolution in brine and,

99   eventually, the rate of CO_2 entry into the caprock.[12,24,26,29,30,33,39,41,59,61–63] Here, we focus

100   primarily on the k_v values of seals. Existing data indicate that $P_{c,b}$ tends to increase by roughly

101   one order of magnitude for every three orders of magnitude decrease in k_v.[64,65]

102   At the regional scale, the effective k_v values of seals are determined by fluid flow through

103   preferential flow paths such as faults, fractures, micro-fractures, and poorly cemented

104   wells.[26,32,45,56,62,66–77] These preferential flow paths, though ubiquitous, do not preclude

105   stratigraphic trapping as shown by the existence of natural CO_2 and hydrocarbon accumulations

106   in the subsurface.[78,79] Evidence of fluid flow through fractures and faults in shales and

107   mudstones—the fine-grained lithologies that constitute the vast majority of aquitards and

108   caprocks to GCS sites and natural gas reservoirs[13,80,81]—is provided by observations of thermal,

109   salinity, and isotopic anomalies near faults,[82–84] of fault and fracture mineralization by

110   carbonates, sulfates, or other solids,[67,76,85,86] and by studies showing that the regional

111   permeability of these formations is sometimes several orders of magnitude higher than k values

112   measured in unfractured core samples.[26,67,87] Conversely, concentration profiles of conservative

113   tracers (halides, noble gases, water isotopes) in shales and mudstones on length scales of tens to

114   hundreds of meters, the persistence of hydraulic pressure differences across these formations,

115   and the scale-independence of permeability in some shales are consistent with molecular

116   diffusion being the dominant mass transport process in these formations on time scales of

117   millions of years.[73,82,84,87,88] Furthermore, while fault damage zones in crystalline rocks tend to

118   have k values orders of magnitude higher than the undamaged rock,[89,90] the mass transport

119   properties of fault damage zones in shale and mudstone are, at least in some cases,

120   indistinguishable from those of the rock matrix.[82,84,91]

121   The presence of faults and fractures in seals, even if they cause only a minor enhancement of

122   seal permeability prior to CO_2 injection, implies that models that describe the seals as

123   homogeneous may underestimate the sensitivity of k_v and $P_{c,b}$ to geochemical and geomechanical

124   alteration.[31,39,63,71,74,75,92–96] Three lines of evidence indicate that clays and clay minerals play an

125   important role in this sensitivity. Firstly, conventional hydrocarbon exploration studies have

126   found that, despite the structural and petrophysical complexity of faults,[66,90,97,98] the barrier

127   properties of faults are primarily determined by the clay content of the fault-filling material as

128   quantified by proxies such as the shale gouge ratio (SGR).[62,98–101] With increasing clay content or

129   SGR, fault permeability decreases from ~10^{-15} to 10^{-19} m^2 and $P_{c,b}$ increases from ~0.1 to 10

130   MPa.[98,100] Secondly, the fault friction coefficient μ_s of the Mohr-Coulomb failure model, an

131   important parameter in the brittle failure of rocks and the mechanics of slip along faults and

132   fractures,[10,35,68,102–104] depends strongly on clay content: μ_s values range from 0.6 to 0.85 for most

133   rocks,[27,104,105] but clay-rich rocks can have μ_s values as low as 0.2.[31,39,97,99,106–109] Clay-rich rocks

134   also tend to deform in a more ductile, self-sealing manner than other rocks, a desirable seal

135   property.[81,85,99,107,110] Finally, the stress-porosity-permeability relations of porous media (or

136   stress-aperture-permeability, in the case of unfilled fractures), of key importance in predicting

137   the permeability of preferential flow paths in seals,[27,78,85,111] are highly sensitive to clay

138   content.[80,112,113] For example, the permeability k of sedimentary rocks is routinely modeled as

139   having a power-law dependence on porosity ϕ,

140   $$k \propto \phi^n,\tag{1}$$

141   where $n \sim 3$ in homogeneous, non-clayey media and larger n values are associated with emergent

142   phenomena such as wormhole-like or bedding-oriented dissolution paterns[34,56,111,114–116] or

143   localized salt precipitation.[53,117] The presence of clay minerals, however, can decrease k by up to

144   five orders of magnitude at fixed porosity[80,87,99,113,118] in a manner that depends strongly on the

145   type of clay mineral (k decreases from kaolinite to illite to smectite).[99,106,119,120]

146   Knowledge of the properties of shales and mudstones lags behind that of other sedimentary

147   rocks despite their importance in a range of areas including basin modeling,[68,77,121–123]

148   radioactive waste management,[73,88,124] wellbore stability,[125–127] soil science,[128] fault rupture,[97] the

149   behavior of subduction zones,[108,129] and the subsurface retention of hydrocarbons.[78,112] The

150   relative scarcity of experimental data on these rocks derives in part from the significant

151   challenges associated with their fine-grained nature. Sample alteration during core retrieval and

152   storage (in particular, the formation of micro-cracks associated with unloading and drying) may

153   not be entirely avoidable.[78,102,118,130–135] Porosity and pore structure are challenging to

154   characterize, because most of the pore space is located in pores with widths between 2 and 10

155   nm, beyond the range of standard microscopy tools, and a significant fraction is located in pores

156   narrower than 2 nm that are not probed by N_2 adsorption or mercury intrusion porosimetry

157   (MIP).[69,77,78,118,131,133,134,136–142] Examination of the microstructure of shales and mudtones

158   increasingly relies on nanoscience tools such as small angle neutron scattering (SANS).[143–145]

159   Studies of mudstone and shale routinely report the clay content of the solid (mass fraction of

160   particles < 2 μm in diameter) but less frequently its clay mineralogy (mass fraction of clay

161   minerals).[77,118,122,146,147] Experimental challenges associated with sample preservation,

162   geomechanics, and the characterization of clay mineralogy are particularly crucial, because the

163   porosity, permeability, and geomechanical properties of clayey media are highly sensitive to clay

164   mineralogy, the stress history of the rock, and the solution with which the rock is in

165   contact.[87,99,102,106,109,112,118,120–122,128,130,133,140,147–150] Finally, measurements of k_v and $P_{c,b}$ are

166   challenging because of their sensitivity to minute leaks and to the compressibility of the testing

167   equipment[83,87,88,151] and because they require durations on the order of weeks to months.[64,65,78,151]

168   Despite the challenges outlined above, a significant database now exists on the core scale

169   relations between ϕ, k_v, and other properties in well-characterized shales and mudstones. Our

170   compilation of existing data on these relations is shown in Figure 2.

171

172

173
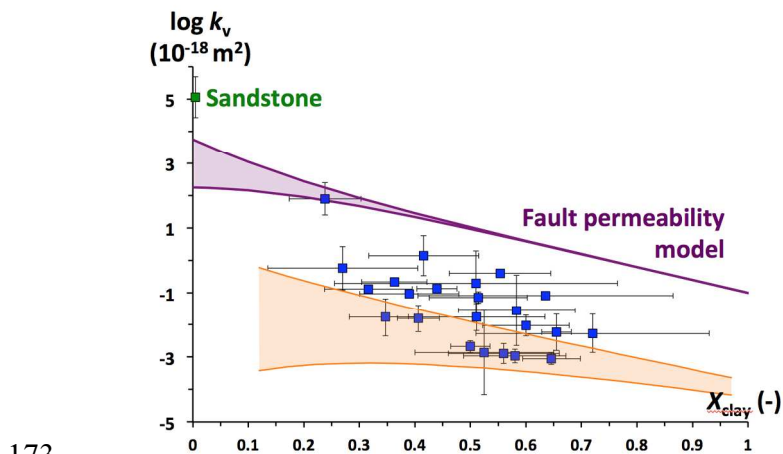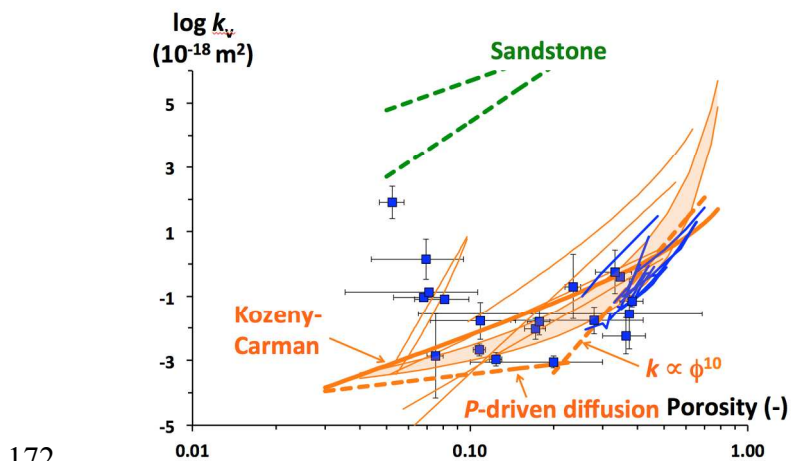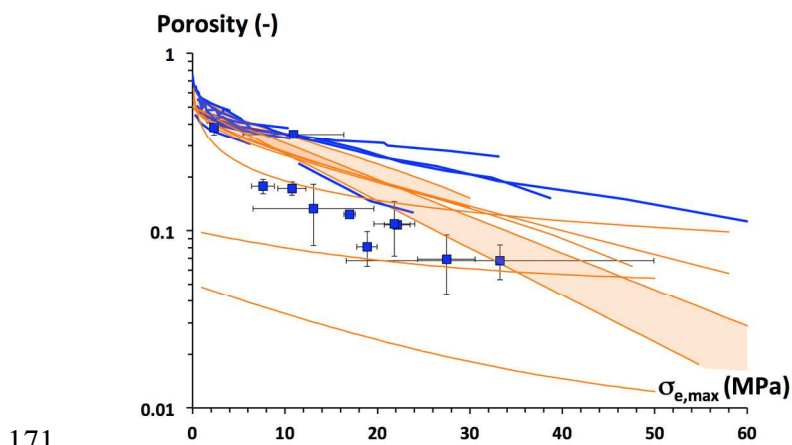
174   **Figure 2.** Compilation of experimental data (blue) and model predictions (orange) on the core

175   scale properties of shales and mudstones: (a) porosity ϕ as a function of maximum effective

176   stress $\sigma_{e,max}$; (b) logarithm of the permeability k_v as a function of porosity; (c) log k_V as a

177   function of phyllosilicate mass fraction X_{clay} in the solid phase. Blue squares represent well-

178   characterized shales and mudstones (Keuper claystone, Kirtland formation, Nordland shale,

179   Draupne shale, Fjerritslev formation, Norwegian shelf Jurassic mudrocks, Chimney Rock and

180   Gothic shale, ZeroGen shale, Tuscaloosa mudstone and marine shale, Boom clay, Toarcian-

181   Domerian shale, Opalinus clay, Callovo-Oxfordian clay, Couche Silteuse, Muderong shale,

182   North German Basin claystones, Wilcox shale, Kimmeridge shale, Floyd shale, Chattanooga

183   shale, Conasauga shale, Duvernay shale, Wakkanai mudstone).[64,67,73,82,84–86,91,102,110,130–132,135–

184   [137,139–142,148,149,152–183] Thick blue lines show a representative selection of normally-consolidated

185   clay-rich sediments either retrieved from a range of depths or compacted to a range of ϕ values

186   using a standard oedometric test.[109,123,146,150,184,185] Permeability values were measured by water

187   advection at the core scale in the direction normal to the bedding or in an unspecified direction.

188   In the case of hydrocarbon-bearing shales, very few hydraulic permeability data are available;

189   helium permeability values were included if they had been obtained on samples pre-treated to

190   remove all other fluids.[183] Porosity values were obtained using techniques that measure the total

191   (water accessible) porosity of nanoporous rocks (HTO diffusion, pycnometry, SANS). Maximum

192   effective stress values were approximated from the maximum burial depth of each formation,

193   d_{max}, using the relation $\sigma_{e,max} \approx 10.9 \times d_{max}$ (with d_{max} in km and $\sigma_{e,max}$ in MPa, based on a solid

194   density of 2.64 kg dm^{-3} and a sediment porosity of 0.2). Orange lines are models of the properties

195   of generic shales and mudstones used in GCS or basin models.[80,86,186–192] The model of

196   Dzevanshir et al.[189] is plotted for clay contents of 40 to 60 % and a sediment age of 170 Ma

197   (lower shaded area in Fig. 2a). The models of Yang and Aplin[80,122] are plotted for clay contents

198   of 40 to 60 % (upper shaded area in Fig. 2a, shaded area in Fig. 2b) and for ϕ = 0.05 to 0.2

199   (shaded area in Fig. 2c). The dashed green lines in Fig. 2b are models of the permeability of

200   generic sandstones.[34,56] The green symbol in Fig. 2c shows the range of sandstone permeabilities

201   predicted by the same models if ϕ = 0.1. The solid purple lines in Fig. 2c describe a model of the

202   relationship between fault permeability and SGR, plotted under the assumption that SGR is a

203   reasonable proxy for X_{clay} (the purple shaded area shows the range of values predicted for fault

204   displacements of 1 mm to 1 km).[98,100]

205

206   Figure 2 reveals that shales and mudstones follow a complex set of relationships between

207    $\sigma_{e,max}$, ϕ, X_{clay}, and k_v. The scatter in the experimental database may reflect the experimental

208   challenges noted above, as well as differences in mineralogy and in the extent of cementation

209   and clay mineral recrystallization.[77,170,172,193] In the case of Fig. 2a, additional scatter may arise

210   because pore water in clay formations can be significantly over- or under-pressured and, also,

211   because ϕ depends not only on $\sigma_{e,max}$ but also, to a smaller extent, on σ_e.[88,129,172,184,189,192] The

212   offset between the properties of weakly consolidated sediments (blue lines) and rocks (blue

213   squares) in Figure 2a suggests that the relation between ϕ and $\sigma_{e,max}$ is sensitive to the rate of

214   compaction, perhaps because slower compaction allows more extensive cementation or because

215   the rate at which pore water can be expelled from compacting fine-grained sediments is limited

216   by the very low permeability of these sediments.

217   The database on k_v vs. ϕ reveals that weakly consolidated sediments roughly follow Eq. 1 with

218    $m \sim 10$ (thick dashed orange line at ϕ > 0.2 in Fig. 2b). This large ϕ-dependence of k_V is

219   consistent with observations that the pore size distribution of shales and mudstones is bimodal or

220   more complex and that compaction tends to compress large, hydrodynamically active pores

221   before nanopores.[77,194,195] At $\phi < 0.2$, the ϕ-dependence of k_v becomes essentially nil (in fact, k_V

222   may have an inverse ϕ-dependence at $\phi < 0.1$ in Fig. 2b), suggesting the disappearance of

223   hydrodynamically active pores. In contrast, almost every model in Fig. 2b, including the well

224   known Kozeny-Carman relation (plotted as a thick orange line in the case of an idealized shale

225   consisting of 20-nm-thick illite particles),[195] predicts a near-linear relation between log k_v and log

226   ϕ. The only exception is the model of Yang and Aplin,[80] a parametric relation fitted to

227   experimental results and describing k_v as a function of ϕ and X_{clay}, which correctly predicts the

228   near invariance of k_V with ϕ at $\phi < 0.2$. This near invariance is consistent with the concept of

229   critical depth of burial (CDB) used in hydrocarbon exploration, according to which the

230   permeability of clayey rocks rapidly decreases with depth until ~2.5 to 3.2 km, then become

231   almost invariant with depth.[78] The near invariance of k_V with porosity at $\phi < 0.2$ may be partly

232   explained by the thick dashed orange line at $\phi < 0.2$ in Fig. 2b, which represents the water flux

233   that would occur by pressure-driven molecular diffusion, i.e., diffusion driven by the P-

234   dependence of the chemical potential of water, calculated here with the equation $k_{v,app} =$

235    $(\mu v_m/RT) \times D_e$, where D_e is the effective diffusion coefficient of water in the porous medium,

236   modeled with the expression $D_e = (\phi/G) \times D_0$ ($\mu = 8.935 \ 10^{-4}$ Pa s is the viscosity of water at 298

237   K, $v_m = 18.07 \ 10^{-6}$ m^3 mol^{-1} is the partial molar volume of water at 298 K, $R = 8.314$ J mol^{-1} K^{-1}

238   is the ideal gas constant, $T = 298$ K is absolute temperature, $D_0 = 2.30 \ 10^{-9}$ m^2 s^{-1} is the self-

239   diffusion coefficient of pure liquid water at 298 K,[196] and $G \sim 4$ is the average geometric factor

240   of smectite-rich porous media).[197] This pressure-driven molecular diffusion model imposes a

241   lower boundary on the range of measureable k_v values, in agreement with Fig. 2b.

242   The plot of log k_v vs. X_{clay} (Fig. 2c) demonstrates that X_{clay} plays an important role in the

243   permeability of shale and mudstone. The data compiled in Figure 2c indicate that k_v decreases by

244   six orders of magnitude as X_{clay} increases from 0 to 0.35 and by one more order of magnitude as

245   X_{clay} increases from 0.35 to 0.7. The database on k_v vs. X_{clay} is roughly consistent with the model

246   of Yang and Aplin[80] but different from the relation between fault permeability and SGR

247   observed at the reservoir scale (thick purple lines).[98,100] This difference may reflect a scale

248   dependence of permeability resulting from the heterogeneous distribution of clays in faults.[97]

249   The much greater sensitivity of k_v to X_{clay} at $X_{clay} < \sim 0.35$ (Fig. 2c) is consistent with several lines

250   of evidence, including data on k_v vs. X_{clay} in clay-sand mixtures,[86] on the mechanics of fracture

251   slip,[198] and on the $P_{c,b}$ values of hydrocarbon fluids in faults,[62,98,101] indicating the existence of a

252   threshold in rock properties at $X_{clay} \approx 0.3$ to 0.4. The location of this threshold is consistent with

253   the predictions of a simple conceptual model of sedimentary rocks as mixtures of large grains

254   (quartz, feldspar, carbonates) and a fine-grained clay matrix, on which an optimal packing of the

255   clay matrix in the space between the larger grains occurs at $X_{clay} \sim 0.35$.[99]

256   Several notable implications of Fig. 2 are, firstly, that models of the stress-porosity-

257   permeability relationships of seals and seal fault zones used in reservoir scale GCS

258   models[27,103,186–188] bear little resemblance to the experimental database. The model of mudstone

259   permeability as a function of ϕ and clay content proposed by Yang and Aplin,[80] which has not

260   been used in GCS models to our knowledge, is the most closely consistent with the experimental

261   database. Field scale simulations that use fixed values of seal porosity and permeability almost

262   invariably assume ϕ values near the lower end of the experimental range ($\phi = 0.01$,[27,47,103,188]

263   0.05,[61,187] 0.05 to 0.07,[35] 0.1,[199] or 0.338)[200] and k_v values near the upper end of the experimental

264   range ($k_v = 10^{-19}$,[27,187,188] 10^{-18},[29,35,47,61,200] $1.6 \ 10^{-18}$,[94] $2.0 \ 10^{-18}$,[199] or 10^{-17} m²).[40,201] Clearly, the

265   values of ϕ and k_v used in field scale GCS models should be reexamined in the light of the

266   experimental database. Secondly, fractures and faults may not strongly impact seal permeability

267   if they are filled by a material with $\phi \leq 0.2$ and $X_{clay} > 0.35$. Thirdly, CO_2-induced dissolution of

268   carbonate minerals in fractures and faults, which is predicted by reactive transport modeling

269   studies and observed in core scale experiments,[94,202,203] may have positive or negative impacts on

270   permeability depending on the values of ϕ and X_{clay} in the fracture- or fault-filling material. In

271   some conditions, carbonate dissolution may even result in a permeability decrease, if the increase

272   in ϕ is more than offset by the associated increase in X_{clay}.

273   Much of the existing core scale research on the evolution of preferential flow paths in seals

274   exposed to CO_2-brine mixtures has focused on open fractures in seal rocks[93,96,203–205] and well

275   cements.[70,206–213] The stress-aperture-permeability relations that determine fluid flow in fractured

276   rocks are analogous to the stress-porosity-permeability relations that describe flow in filled

277   fractures.[86,135,214] The few existing data on these stress-aperture-permeability relations in the case

278   of shales and mudstones suggest that fractures can self-seal on time scales of days to months if

279   σ_e is sufficiently high.[85,86] The precise stress-dependence of k_v and $P_{c,b}$ in seal fractures,

280   however, is not well known, because of insufficient understanding of the mechanics of asperities

281   on fracture surfaces and of the feedbacks between the mechanics of the fracture and of the rock

282   matrix.[81,85,86,135,155,174,215,216]

283   In the case of CO_2 invasion in fractured caprocks, two important complications are the

284   importance of crack dilation mechanics on two phase flow in argillaceous rocks[171,214,216] and the

285   geochemical alteration of fracture surfaces by CO_2. Existing studies show that CO_2-brine

286   mixtures can rapidly dissolve calcite (and, in the case of cement, portlandite) on fracture surfaces

287   if the invading brine is undersaturated with respect to calcite, rapidly increasing fracture

288   aperture, generating a higher-porosity altered zone on fracture surfaces and also, at least in some

289   cases, increasing fracture surface roughness.[70,93,96,203–205,210,211] If the invading fluid is

290   equilibrated with respect to calcite, the reactivity of fracture surfaces is much slower and

291   dissolution of M^{II}-bearing silicates followed by precipitation of carbonates and amorphous silica

292   can result in fracture sealing in certain conditions, particularly at low fluid flow

293   rates.[70,74,207,209,212,213,217–222] Important unknowns in models of geochemical fracture alteration

294   include the impact of adsorption[162,223] and porosity changes[208,224] on molecular diffusion

295   coefficients in the rock matrix. In some cases, calcite dissolution on fracture surfaces has been

296   found to lead to the release of colloidal particles (clays, dolomite) and a decrease in fracture

297   permeability,[93,96,204,205] a behavior analogous to that hypothesized for filled fractures in the

298   previous paragraph based on the data in Figs. 2b,c. Finally, geochemical alteration has been

299   found, at least in some cases, to weaken fracture surfaces and asperities by dissolving carbonate

300   and silicate cements, modifying the stress-aperture relationship of the fracture in a manner that

301   facilitates fracture sealing by normal stresses. [39,71,205,213,219]

302   The sensitivity of seals to geochemical and geomechanical alteration elicits several important

303   fundamental questions. One of these questions is the manner in which carbonates precipitate in

304   fractured nanoporous rocks. Nanoscale studies of this phenomenon reveal that the kinetics of

305   carbonate precipitation are strongly influenced by the substrate on which they precipitate,[225,226]

306   the roughness of the substrate,[227] the presence of adsorbed water films,[228] and pore size.[229–232]

307   These studies suggest that in fractured seals, carbonate solids may sometimes preferentially

308   precipitate in the fractures rather than in the nanoporous rock matrix, a phenomenon that may be

309   driven by the surface energy of carbonate minerals[229,233] and that would enhance the resilience of

310   seals to geochemical alteration.

311   A second key nanoscale question is the impact of geochemical alterations on the mechanics

312   (swelling, aggregation) and permeability of seals. The mechanics of clayey media are well

313   known to be sensitive to ionic strength, pH, and the valence of the exchangeable

314   cation[120,121,124,126,234–236] in a manner that reflects the role of pore fluids in hydrating clay surfaces

315   and in mediating electrostatic interactions between clay particles.[120,125,234,235] This sensitivity

316   strongly impacts the permeability and mechanics of weakly consolidated clays,[124,195] but the

317   effect on shale and mudstone is variable and has not been systematically examined at GCS-

318   relevant conditions of high salinity, effective stress, and, pCO_2.[77,127,142,149,237] In this context,

319   recent observations that smectite-water pastes can adsorb significant quantities of CO_2 (up to

320   ~0.07 g_{CO2} g_{clay}^{-1} at high pCO_2 levels) by intercalation of CO_2 in water-filled clay interlayer

321   nanopores, and that this intercalation modifies the swelling free energy of the clay minerals, may

322   be highly relevant (it also implies that clay-rich seals can be viewed, to some extent, as storage

323   formations).[173,238–243] This CO_2-induced alteration of clay mechanics may impact fracture

324   apertures and the frictional strength of clay-rich fault gouge,[239] but a detailed understanding of

325   the relationships and their relevance to seal permeability remain to be established.

326   **Residual trapping: residual CO_2 saturation ($S_{g,r}$) in reservoir rocks.** Residual CO_2

327   saturation ($S_{g,r}$) is a key parameter of GCS models that determines the extent of residual trapping

328   and strongly influences plume migration velocity, storage capacity, and storage

329   security.[4,14,23,24,41,244,245] Despite its importance, $S_{g,r}$ remains poorly constrained and a large range

330   of values have been used in field scale models (solid and dashed lines in Fig. 3). The

331   experimental database on $S_{g,r}$ in GCS-relevant conditions includes only a handful of field scale[246]

332   and core scale measurements,[244,247–257] some of which may be highly uncertain.[16,258] Current

333 understanding of $S_{g,r}$, therefore, remains strongly influenced by studies of non-aqueous fluids

334 other than CO_2.[259–267]

335 Investigations of residual trapping of CO_2 and hydrocarbons indicate that $S_{g,r}$ is highly

336 sensitive to the initial CO_2 saturation $S_{g,i}$ and the mineral-water-CO_2 wetting angle θ (defined

337 such that $\theta = 0°$ for a perfectly hydrophilic medium).[252,254] The capillary number $Ca = v_w\mu_w/\gamma_{gw}$

338 (where v_w and μ_w are the Darcy velocity and viscosity of the aqueous phase and γ_{gw} is the CO_2-

339 water interfacial tension) also influences $S_{g,r}$, but only at high fluid velocities ($Ca > 10^{-6}$) that are

340 not relevant to CO_2 trapping in GCS.[33,252,268] Details of multiphase flow at the pore network to

341 core scale have a less well-characterized influence on $S_{g,r}$ that may result in a dependence of $S_{g,r}$

342 on ϕ.[253,254,260,262,269] The yellow and blue diamonds in Fig. 3 are consistent with $S_{g,r,max}/S_{g,i,max} =$

343 $0.166/\phi^{0.63}$, where $S_{g,i,max}$ and $S_{g,r,max}$ are the maximum achievable initial and residual CO_2

344 saturation.[253] Residual CO_2 saturation $S_{g,r}$ also depends on pore to core scale heterogeneity[253,270]

345 and on the topology of the CO_2 phase.[269,271] Other properties that influence $S_{g,r}$, such as CO_2-

346 brine interfacial tension γ_{gw},[248] are thought to do so primarily through their impact on $S_{g,i}$ or θ.

347

348
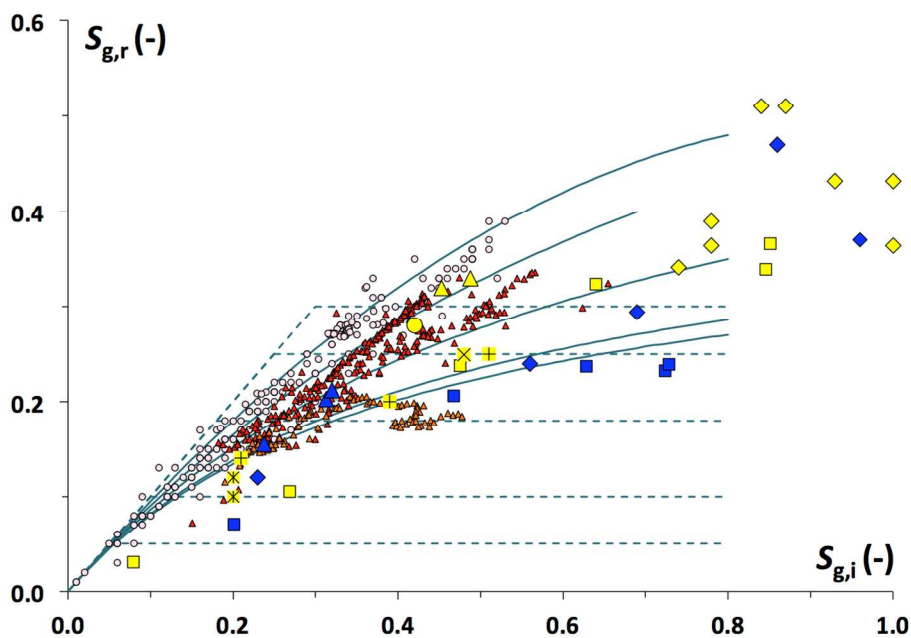
Figure 3. Plot of $S_{g,r}$ vs. $S_{g,i}$ measured in core samples or reservoir rocks at Ca $\leq 10^{-6}$ (symbols) or used in field scale GCS models (lines). Experimental results obtained at unspecified $S_{g,i}$ or Ca conditions or with brine that was not initially saturated with respect to CO_2 are not shown.[244,247,248,272] Small red and orange triangles were obtained in sandstone at the scale of an X-ray CT voxel (red: Berea, Paaratte, Tuscaloosa; orange: Mount Simon).[252] Small pink circles were obtained in Berea sandstone (at Ca $\leq 2.5\ 10^{-6}$) at the scale of an X-ray CT slice.[273] Yellow symbols were obtained in sandstone at the core scale (cross (x): Doddington;[249] crosses (+): Berea;[256] asterisks (✳): Berea;[269]; squares: Berea;[250] circle: Tako;[251] diamonds: Berea, Doddington, Stainton, Springwell;[253] triangles: Bentheimer, Doddington).[255] Blue symbols were obtained in limestone at the core scale (diamonds: Ketton, Estaillades, Indiana;[253] squares: Indiana;[257] triangles: Estaillades, Ketton, Mount Gambier).[255] Solid lines describe models based on Land's formulation $\{S_{g,r} = S_{g,i}/(1+CS_{g,i}),$ where C is Land's constant$\}$[259] with $C = 2.45,$[24] $2.25,$[59] $1.61,$[274] or 1.05[23] or based on the model of Spiteri and coworkers[267] $\{S_{g,r} = \alpha S_{g,i} - \beta S_{g,i}^2\}$ with $\alpha = 1$ and $\beta = 0.5.$[275] Dashed lines describe models according to which $S_{g,r}$ equals $S_{g,i}$ up to a

363   certain value and is invariant with $S_{g,i}$ above this threshold value, with $S_{g,r,max} = 0.05$,[28,36,103,186–

364   188,202] 0.10,[60] 0.18,[276] 0.25,[26,35,41,61,200] or 0.30.[40] For clarity, the dashed lines are drawn with

365    $S_{g,i,max} = 0.8$. Models of $S_{g,r}$ that used almost identical values of $S_{g,r,max}$ are shown as a single line.

366   Well-based measurements at the Otway GCS pilot site yielded $S_{g,r} = 0.11$ to 0.2, but the

367   corresponding $S_{g,i}$ value was not reported.[246]

368

369   The dependence of $S_{g,r}$ on $S_{g,i}$ and θ has been extensively examined at the core and pore-

370   network scales in the case of hydrocarbon-water systems.[259–261,263–267] In strongly hydrophilic

371   media, $S_{g,r}$ increases monotonically with $S_{g,i}$ to a maximum value $S_{g,r,max}$.[259,267] In mixed-

372   wettability systems, $S_{g,r}$ is smaller than in water-wet systems and may have a non-monotone

373   dependence on $S_{g,i}$.[263,265,267] The influence of θ on $S_{g,r}$ derives from the mechanisms of brine

374   imbibition at the pore network scale: small θ values favor imbibition by a link snap-off

375   mechanism (i.e., by filling of pore throats in order of increasing size, which traps the non-wetting

376   phase in the pore bodies), whereas larger θ values favor imbibition by piston-type displacement,

377   which causes less trapping.[260,264,266,267]

378   Models of $S_{g,r}$ in GCS-relevant conditions evidently require accurate predictions of $S_{g,i}$ and θ in

379   mineral-brine-CO_2 systems. Capillary invasion in porous media, which determines $S_{g,i}$, is a

380   complex, multi-scale phenomenon that is largely beyond the scope of this review.[50,277,278] Here,

381   we focus on the mineral-brine-CO_2 wetting angle θ, and in particular on the θ values obtained as

382   the water phase recedes or advances, θ_r and θ_a, a fundamental property that remains incompletely

383   understood in the context of GCS. Core scale measurements of capillary pressure vs. CO_2

384   saturation (P_c vs. S_g) and X-ray CT images of fluid distribution during CO_2-brine multiphase

385   flow yield indirect estimates of θ when interpreted with the Young-Laplace equation,

386     $P_c = C\,\gamma_{gw}/r_t \times \cos\theta,$ (2)

387   where P_c is the capillary pressure at which CO_2 can invade pore throats of radius r_t, γ_{gw} is the

388   CO_2-water interfacial tension, and C is a shape factor equal to 1 for slit-shaped pore throats and 2

389   for circular pore throats. Capillary invasion studies show that GCS relevant rocks and minerals

390   are water-wet during CO_2 invasion ($\theta_r \sim 0$ to $50°$).[51,250,268,278–281] During brine imbibition, most

391   measurements yield high $S_{g,r}$ values and a monotone dependence on $S_{g,i}$ indicative of water-wet

392   systems (Fig. 3). However, three types of data suggest that GCS-relevant rocks may be

393   intermediate-wet during brine imbibition ($\theta_a \sim 90°$), at least in some cases: firstly, data on $S_{g,r}$ in

394   Mount Simon sandstone, where many sandstone grains are coated with fibrous illite, show less

395   trapping and a non-monotone dependence on $S_{g,i}$ suggestive of intermediate-wet conditions

396   (orange triangles in Fig. 3).[252] Secondly, several studies of brine imbibition in quartz and

397   carbonate sand packs report low P_c values suggestive of intermediate-wet properties.[247,272,281]

398   Thirdly, pore-network scale examinations of the distribution of CO_2-brine fluid mixtures in sand

399   packs and glass micromodels suggest that silica surfaces sometimes become intermediate-wet

400   upon exposure to CO_2.[249,254,282] These observations highlight the need for predictive models of

401   wettability and contact angle hysteresis in CO_2-brine-mineral systems such as those that already

402   exist for oil-water systems.[283]

403   Direct measurements of θ using micromodels,[282] goniometric contact angle

404   experiments[49,245,284–300] and molecular dynamics (MD) simulations[301–305] provide little clarity on

405   the wetting properties of rocks exposed to CO_2. As expected, carbon-rich solids such as

406   anthracite, limestone from the Weyburn oilfield, and oil-coated quartz, and partly

407   dehydroxylated silica surfaces have intermediate-wet properties ($\theta = 44$ to $140°$).[284–

408   286,288,301,303,305] Other solids (calcite, silica, clays, mica), however, have θ values ranging from

409   water-wet to intermediate-wet (θ = 0 to 100°) depending on the study.[49,245,282,288–291,293–

410   300,302,303,306]

411   Figure 4 shows a compilation of all available data on the θ_r and θ_a values of mineral-brine-CO_2

412   systems obtained in goniometric contact angle experiments, excluding results that were obtained

413   with dehydroxylated silica surfaces. Studies that did not impose an advancing or receding water

414   phase, not shown in Fig. 4, yielded θ values that were mostly intermediate between the θ_r and θ_a

415   values compiled in Fig. 4, as expected.[288,291,293,302,305] The data compiled in Fig. 4 yield average

416   θ_r values of 21 ± 11°, 25 ± 16°, and 30 ± 8° for quartz, calcite, and mica, i.e., the mineral

417   surfaces are water-wet during CO_2 invasion. The uncertainty derives primarily from systematic

418   differences between the results of different groups. Possible causes of these systematic

419   differences (and also of the differences between measurements of θ and $S_{g,r}$ obtained from pore-

420   network and core scale experiments) include the sensitivity of θ to trace levels of impurities and

421   differences in surface roughness.[300,307] The difference between the θ_r values of silica in air (0°)[308]

422   and in CO_2 (21 ± 11°) is consistent with the smaller negative surface proton charge of silica at

423   lower pH values.[51,245,282,297,306] Other silicate minerals (feldspars, clay minerals) have similar

424   wettability to quartz, calcite, and mica.[292,297] Reported θ_r have little or no P- or T-dependence.

425   The salinity-dependence may be either positive,[49,295] negative,[297] or essential nil.[294]

426   For all three surfaces, θ_a is significantly larger than θ_r, and the range of θ_a values reported by

427   individual research groups is much larger than the range of reported θ_r values (Fig. 4).[49,294,296,300]

428   Existing data reveal that θ_a increases significantly with salinity (by ~ 5° per M NaCl) with no

429   clear P or T dependence.[49,294,296,300]

430

431
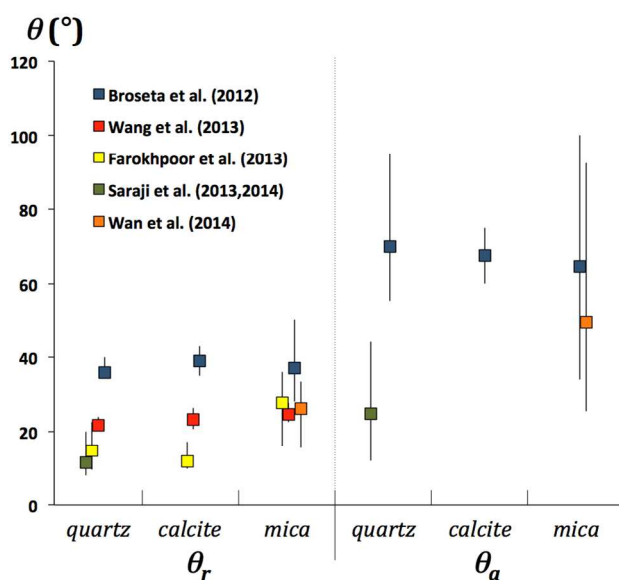
Figure 4. Compilation of the best available measurements of θ in mineral-brine-CO_2 systems measured during water retreat (θ_r) and advance (θ_a) on quartz, calcite, and mica by groups that used a captive CO_2 drop positioned beneath the solid substrate in an otherwise brine-filled reservoir. Results that were obtained with partially or fully dehydroxylated silica surfaces,[284,301,303] with the sessile drop technique,[288,291,293,302] or that did not fully describe their experimental techniques are not shown.[292] Results reported by Broseta et al.[294] include previously published data by the same group.[289,290] Symbols show the average reported values. Vertical lines show the range of measured θ values (not the uncertainty of individual measurements) over the examined pressure, temperature, and salinity range (Saraji et al.[296]: 3.4-11.7 MPa, 308-333 K, 0 M; Saraji et al.[49]: 13.8-27.6 MPa, 323-373 K, 0.2-5.0 M; Farokhpoor et al.[295]: 0.3-40 MPa, 309-339 K, 0-0.8 M NaCl; Wang et al.[297]: 7-20 MPa, 303-323 K, 0-1.15 M Na-Cl-Ca-SO$_4$-Mg brine; Broseta et al.[294]: 0.5-14.0 MPa, 282-393 K, 0-7 M NaCl; Wan et al.[300]: 7.5-15 MPa, 318 K, 0.1 M NaCl).

445

446   At the nanoscale, the θ values of mineral surfaces derive from the interfacial energies of the

447   mineral-brine (γ_{sw}), mineral-CO_2 (γ_{sg}), and brine-CO_2 interfaces through Young's equation:

448    $\cos\theta = (\gamma_{sg} - \gamma_{sw})/\gamma_{gw}$.   (3)

449   The   brine-CO_2 interfacial   energy γ_{gw} has   been   extensively   studied   using

450   experiments,[287,288,296,299,309–314] MD simulations,[303,315–317] and lattice-gas simulations.[318] The

451   experimental database indicates that γ_{gw} decreases with P and increases with T and

452   salinity.[309,310,312,313,315,319] In most GCS-relevant conditions, $\gamma_{gw} \sim$ 25 to 30 mN m^{-1} with little P or

453   T dependence and with a linear salinity dependence of about 1.5 mN m^{-1} per unit of anionic or

454   cationic charge molality.[287,288,296,303,311,314,316] Theoretical studies have shown that the P- and

455   salinity-dependence of γ_{gw} results from CO_2 adsorption and salt exclusion at the brine-CO_2

456   interface in accordance with the Gibbs adsorption equation:[303,315,317–319]

457    $d\gamma_{gw} = -\Gamma_i^{(w)}d\mu_i$,   (4)

458   where μ_i is the chemical potential of species i and $\Gamma_i^{(w)}$ is the surface excess of i relative to water

459   at the interface. The absolute values of γ_{sg} and γ_{sw} are not directly measurable,[320] but Eq. 4

460   provides a route towards predicting their P- and salinity-dependence. For example, Eq. 4

461   indicates that adsorbed water films at mineral-CO_2 interfaces (known to exist at least in some

462   conditions)[304,306,321–323] must influence γ_{sg} through the direct influence of water adsorption[324] but

463   also the P-dependence of γ_{sg} through the influence of the water film on CO_2 adsorption at the

464   solid-CO_2 interface. The sensitivity of interfacial energy to adsorption implies that θ must be

465   sensitive to any impurity that adsorbs at any interface in the mineral-brine-CO_2 system,

466   particularly at the CO_2-mineral interface.[11,17,57,279,288] According to Eq. 4 the hysteresis of

467   measured θ values further implies the existence of a hysteretic interfacial reaction. Several

468   studies have hypothesized that this reaction is a strong binding (chemisorption) of CO_2 to surface

469   hydroxyl functional groups.[284,294,296] However, infrared spectroscopy, neutron scattering, and

470   MD simulation results consistently indicate that CO_2 adsorbs on silica, feldspar, and mica

471   surfaces by a weak physisorption mechanism and is completely displaced from these surfaces in

472   the presence of water.[322,325,326] Therefore, the underlying origin of the hysteresis of mineral-

473   brine-CO_2 θ values remains unknown.

474   **Mineral trapping: Reactive surface area (a_r) of silicates at *in-situ* conditions.** Of the four

475   trapping mechanisms involved in GCS, the ultimate and most secure is mineral trapping (Fig. 1),

476   whereby CO_2 is sequestered as solid carbonates through reactions of the type:[42,43,327]

477    $M^{(II)}$-bearing-silicates + CO_2 + H_2O $\Rightarrow$ carbonate minerals + $M^{(II)}$-free-silicates   (5)
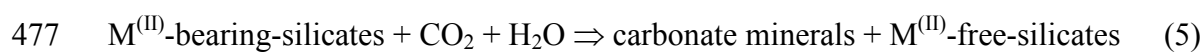
478   In Eq. 5, key $M^{(II)}$-bearing-silicates include feldspars (plagioclase), phyllosilicates (biotite,

479   chlorite, glauconite, smectite), and mafic minerals (olivine, pyroxene); $M^{(II)}$-free silicates include

480   feldspar, kaolinite, and quartz.[42–44,92,116,328,329] Natural analogs and geochemical models indicate

481   that the carbonate minerals responsible for CO_2 trapping are primarily dolomite, ankerite,

482   siderite, and dawsonite.[44,92,202,327,329–332] The rate and extent of mineral trapping are not well

483   understood, largely because of uncertainties in the reactivity of silicate minerals. These

484   unknowns influence predictions of CO_2 mineral trapping, but also CO_2 storage capacity via

485   porosity and permeability evolution[114,116,333–335] and leakage pathway evolution via geochemical

486   alteration of fractured seals and well cements.[45,74,93,336]

487   In field scale GCS models, silicate reaction rates are generally described with the

488   phenomenological transition-state-theory (TST) formalism,[116,232,337] which requires knowledge,

489   for each silicate phase of interest, of its reactive surface area a_r, its thermodynamic solubility

490   constant K_s, and several rate law parameters for each reaction mechanism. For example, the rate

491   of proton-promoted growth (R_H) is described as:

492    $R_H = a_r \left\{ \left[1 - \left(\frac{Q}{K_s} \right)^p \right]^q \right\} \left\{ k_H^{298K} \, e^{-\frac{E_H}{R}\left(\frac{1}{T} - \frac{1}{298K}\right)} (H^+)^{n_H} \right\}$ (6)

493   where the first set of brackets describes the thermodynamic driving force (Q is the ion activity

494   product, p and q are empirical power-law exponents) and the second set of brackets contains the

495   rate law parameters for the proton-promoted reaction mechanism [k_H^{298K} is the rate constant at

496   298 K, E_H is the activation energy, (H^+) is the activity of the proton, and n_H is the reaction order

497   with respect to protons].[43,44,46,338–341] Modeling silicate reaction rates with this formalism has

498   several weaknesses from the functional form of the rate law itself to uncertainties in parameter

499   values. Model parameters are based on laboratory scale measurements of pure mineral phases in

500   simple electrolytes at far-from-equilibrium conditions, thus their accuracy for predicting reaction

501   rates in realistic conditions is highly uncertain, particularly in the case of

502   aluminosilicates.[43,44,46,76,336,342,343] Parameters for Eq. 6 are compiled in thermodynamic and

503   kinetic databases,[344–346] with the choice of database used influencing model predictions of

504   trapped CO_2 by as much as 61%.[347,348] In addition, rate law parameters for mixed mineral

505   phases,[28,349] poorly crystalline phases such as amorphous Si-rich phases,[228,341,350–352] or other

506   phases such as analcime and ankerite[340] are poorly constrained. In these cases, mineral proxies

507   are often used to approximate rate parameters. Selection of an appropriate mineral proxy is not

508   trivial as the resulting approximations can significantly impact predicted mineral reactions.[353]

509   Microstructural details, such as the distribution of Al/Si ordering in feldspars, are often not

510   accounted for and may considerably influence mineral reactivity.[354]

511   Beyond parameter uncertainties, the functional form of Eq. 6 is known, at least in some cases,

512   to overestimate near-equilibrium rates, overestimate the nucleation rate of new mineral phases (it

513   predicts that minerals start to precipitate as soon as $Q > K_s$ even if only by an infinitesimal

514   amount), overestimate growth rates in conditions where the concentration ratios of reactants in

515   solution differ from their stoichiometry in the solid, and require different parameterizations to

516   describe dissolution and growth.[28,116,202,232,355–358] These limitations are due, in part, to the fact

517   that kinetic databases reflect only the range of conditions examined in laboratory experiments

518   and, thus, they inherently cannot predict the possible existence of additional reaction pathways at

519   elevated pCO_2 levels,[359–363] in the presence of H_2S, SO_2, or CH_4 impurities,[336,364] or in the

520   presence of trace ions present in natural brines,[365] or differences between the reactivity of

521   mineral surfaces with water-saturated CO_2 vs. CO_2-saturated water, which is a function of the

522   thickness of adsorbed water films at CO_2-mineral interfaces.[228,321,351,366–371] Improved predictions

523   of mineral growth rates have been demonstrated using new rate laws,[232,356] but a consistent

524   framework applicable in reactive transport simulations has yet to emerge. Finally, the precision

525   of Q values used in Eq. 6 remains limited by incomplete knowledge of solution chemistry in

526   CO_2-rich brines, particularly with regard to aluminum geochemistry and the activity coefficients

527   of solutes at high ionic strength (> 1 M).[42,43,372,373]

528   While much attention has been devoted to the challenges described above regarding rate law

529   parameterization, a more pervasive source of uncertainty in applying Eq. 6 to rocks resides in the

530   specific reactive surface areas a_r of each mineral phase.[46,329,356] Reactive transport models often

531   approximate a_r with the specific surface area, a_s, that can be measured for pure minerals, for

532   example, using the Brunauer-Emmett-Teller (BET) gas adsorption technique,[374] or estimated as

533   the geometric surface area assuming one or more particle sizes and a smooth[340,375–377] or rough

534   surface modified with a surface roughness factor.[378–380] Reactive surface area also depends on the

535   fraction of the specific surface area that is not occluded by surface coatings or other mineral

536   grains, referred to as the specific accessible surface area of each mineral phase, a_a.[381] These

537   surface areas are related to each other by scaling factors C_1 and $C_2 < 1$:

538 $a_r = (C_1)\, a_a = (C_1 C_2)\, a_s$ (7)

539 where C_2 describes the fraction of the specific surface area that is accessible, and C_1 describes

540 the fraction of the accessible specific surface area that is reactive. In practice, these scaling

541 factors are either assigned an arbitrary value ($C_1 C_2 = 10^{-3}$ to 10^{-1},[28,42,43,382] $C_2 = 10^{-3}$)[349,364] or

542 adjusted to fit measured reaction rates.[338,383] The range of a_r values used in field scale GCS

543 models for a selection of common minerals is shown in Fig. 5. To a first approximation,

544 increasing or decreasing all a_r values by a scaling factor has the same effect as scaling the time-

545 axis of mineral reactivity with CO_2 by the same factor.[20,42] Therefore, the range of a_r values in

546 Fig. 5 generates roughly two to four orders of magnitude uncertainty in the time scale of mineral

547 trapping.

548
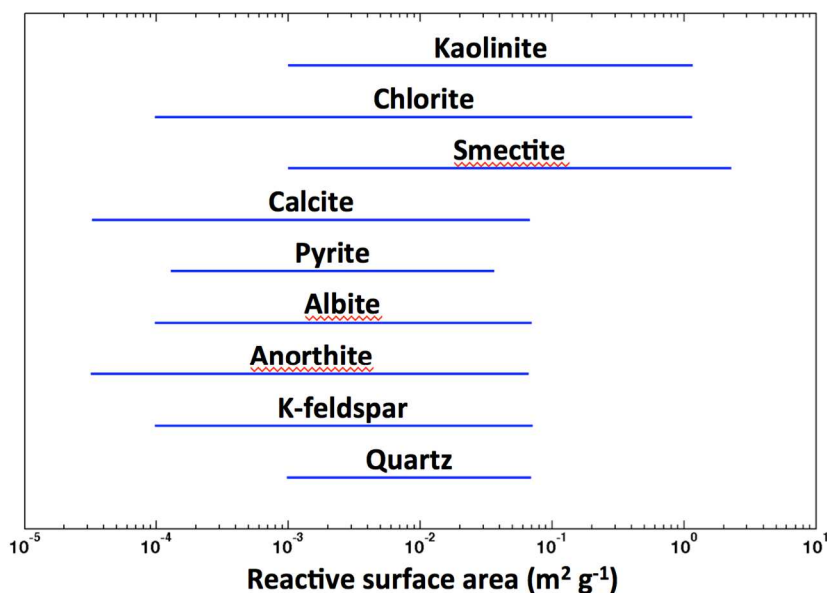
549

550 **Figure 5.** Compilation of a_r values used in field scale GCS models for a selection of common

551 minerals.[38,42,202,340,377–380,383–390]

552

553   Microscopic scale studies can provide important constraints for the parameterization of the

554   scaling factors in Eq. 7.[116] Examinations of geochemical alteration rates in pore network models,

555   core scale experiments, and reactive flow experiments show that the scaling factors are not

556   invariant with time, aqueous chemistry, flow rate, or surface topography[232,391–394] as frequently

557   assumed in field scale GCS models. At the nanoscale, reaction rates may depend more closely on

558   reactive site density than on reactive surface area.[232,394] At the microscopic scale, examinations

559   of sandstones and limestones show that C_2 is mineral-specific (i.e., mineral accessibility does not

560   reflect bulk mineral abundance) because clay minerals tend to form surface coatings and cements

561   in the framework of larger quartz and carbonate grains.[144,381,395,396] Furthermore, C_2 depends on

562   the scale of observation; for example, in one study of chlorite clay coatings and pore-filling

563   cements in sandstone, coatings that appeared continuous at a ~1 μm resolution were found to be

564   porous at a ~10 nm resolution.[395]

565   Surface coatings are particularly critical in the evaluation of a_r, because they diminish the

566   reactivity of the underlying solid by several orders of magnitude in some cases, such as

567   amorphous Si-rich coatings on feldspar, olivine, and borosilicate surfaces, kaolinite coatings on

568   feldspar surfaces[397–401] while leaving it essentially unchanged in other cases like smectite

569   coatings on feldspar surfaces, calcite coatings on diopside and basaltic glass, Mg-rich carbonate

570   coatings on dolostone.[401–405] At present, theory and models for predicting which coatings will

571   impact mineral accessibility and reactivity are lacking. The mode of surface coating precipitation

572   may explain experimental results in some cases, such as epitaxial growth having a greater

573   inhibitory effect than random 3D nucleation and growth,[403,404,406] while in other studies

574   ostensibly identical amorphous Si-rich coatings have different impacts on the reactivity of

575   different samples and even on different faces of the same crystal.[407,408]

576   At the scale of a dissolving mineral surface, the formation of surface coatings is coupled to

577   mineral reactivity not only through its impact on a_r, as noted above, but also through its impact

578   on solution chemistry at the dissolving surface.[409] For example, in near-equilibrium conditions

579   feldspar dissolution may occur an order of magnitude more slowly than in far-from-equilibrium

580   conditions because it is rate-limited by clay mineral precipitation.[358,410] Such coupled reactions

581   may result in a dissolution that is, overall, incongruent, as in the case of dissolving

582   aluminosilicate surfaces.[350,409,411,412] Nanoscale studies suggest that the appearance of non-

583   stoichiometry may, in some cases, involve stoichiometric dissolution followed by the subsequent

584   precipitation of a surface coating,[350,398,409,413] whereas in other cases it involves the release of

585   soluble elements without a full dissolution of the silicate matrix.[414,415] This coupling of mineral

586   dissolution and precipitation rates may be an important factor contributing to the discrepancy

587   between field and laboratory data on mineral weathering rates.[339,410,416]

588

589   **SUMMARY AND CONCLUSIONS**

590   Long-term storage of CO_2 in porous sedimentary formations relies on several properties that

591   have a clear nanoscale basis including the vertical permeability k_v of seals, the residual CO_2

592   saturation $S_{g,r}$ in reservoir rocks, and the reactive surface area a_r of minerals. These parameters,

593   and others, are macroscopic representations of nanoscale physico-chemical interactions that

594   occur at interfaces between mineral grains and fluids, and between coexisting fluids. A review of

595   available data on fluids, minerals, and rock types relevant to geologic carbon storage indicates

596   that the values typically used for these parameters in field scale models are not reflective of the

597   current state of knowledge, but neither is there an adequate understanding of the nanoscale basis

598   for the observed behavior or a means to predict how the behavior might evolve in a chemically

599   reactive system like CO_2-brine-minerals. There is a need to better define the origins of these

600   properties in terms of fundamental physico-chemical interactions, and to develop new

601   constitutive relations to allow these properties to evolve during the extended time period (weeks

602   to millennia) needed to describe CO_2 storage.

603   The seal rocks that cap CO_2 sequestration systems in the subsurface (typically shale and

604   mudstone) present special challenges as a result of their fine grain size and heterogeneity both in

605   terms of texture and mineralogy. Ultimately, to ensure safe CO_2 storage, it is necessary to know

606   the vertical permeability and capillary entry pressure for such rocks, both of which depend on

607   porosity, state of stress, mineralogy, and presence of fractures. In particular, knowledge of the

608   properties of seals is required to develop a more accurate understanding of the sensitivity of seal

609   k_v and $P_{c,b}$ values to geochemical and geomechanical alteration. At present, knowledge of the

610   properties of shales and mudstones lags behind that of other sedimentary rocks, as illustrated by

611   the fact that extant models of the stress-porosity-permeability relations of these rocks bear little

612   resemblance to the experimental database. A first key need is to better understand the impact of

613   clay mineral mass fraction on the stress-porosity-permeability relations of fine-grained rocks and

614   its relation to the microsctructure of fine-grained rocks. Clay minerals can decrease k by more

615   than four orders of magnitude at fixed porosity. A second key need is to understand the impact of

616   clay minerals on fracture permeability and on the sensitivity of fracture permeability to

617   geochemical alteration. Existing data suggest that fractures and faults may not strongly impact

618   seal integrity if they have a sufficiently high clay content, and dissolution of carbonate minerals

619   in fractures and faults may actually result in permeability decrease if the porosity increase is

620   offset by an increase of the clay fraction in the fault. A third key need is to better understand the

621   mechanical response of asperities on fracture surfaces in shales and mudstones to induced

622   stresses, and the impact of geochemical alteration on those responses. Finally, future research

623   should resolve the impact of pore size on the precipitation of secondary carbonate solids and

624   determine the impact of CO_2 adsorption on hydrated swelling clay minerals. In particular, the

625   impact of CO_2 adsorption on fracture apertures and on the frictional strength of clay-rich fault

626   gouge is important.

627   Residual CO_2 saturation ($S_{g,r}$) is a key parameter of GCS models that determines the extent of

628   residual trapping and strongly influences plume migration velocity, storage capacity, and storage

629   security. Residual CO_2 saturation is highly sensitive to the mineral-water-CO_2 wetting angle, θ,

630   but potential changes in θ present difficulties in predicting $S_{g,r}$. Although it is generally believed

631   that GCS relevant rocks are water-wet in the presence of CO_2, there are both conflicting static

632   measurements as well as evidence that exposure of mineral surfaces to CO_2-acidified brine

633   changes wetting behavior for several minerals. In this context, one key need is to measure the

634   sensitivity of core-scale $S_{g,r}$ values to interfacial-scale θ values and the dependence of this

635   sensitivity on rock properties such as surface roughness. A second key need is to determine the

636   timing of the wettability alteration, for example, does it occur when CO_2 first contacts the rock,

637   or does it take place more slowly and primarily influence brine imbibition. Finally, a third key

638   need is to develop predictive models of wettability and contact angle hysteresis in CO_2-brine-

639   mineral systems, which can only come from knowledge of the nanoscale phenomena at the

640   mineral-fluid interface.

641   Although it is generally slow, mineral trapping is of considerable interest because it represents

642   permanent immobilization of the injected CO_2 and, if extensive, lessens the need to make long

643   term predictions of migration of fluid phases in the subsurface. However, the rate and extent of

644   mineral trapping are not well understood, largely because of uncertainties in the dissolution and

645   precipitation rates of silicate minerals. In field scale GCS models, silicate reaction rates are

646   generally described with a phenomenological transition-state-theory (TST) formalism, but this

647   formalism is inadequate for a number of reasons, including its reliance on parametric fits of

648   laboratory data that are determined at far from equilibrium conditions and the need to specify the

649   reactive surface area a_r of each mineral. Viewed at the nanoscale at the mineral surface, mineral

650   dissolution is affected by chemical impurities, coupled reactions, mineral coatings, roughness,

651   and roughness evolution with time. Overall, there is still little predictive capability for mineral

652   reactivity on the long timescales (tens to thousands of years) needed to predict mineral trapping

653   of CO_2. A first key need in this area is the development of advanced rate laws that account for

654   mechanisms and chemical species that are important in GCS-relevant conditions. A second key

655   need is for experimental studies of the properties of surface coatings and their impact on surface

656   reaction rates. Finally, a third key need is to elucidate the pore-network scale feedbacks between

657   flow and reactivity, particularly in conditions with low flow rates that are most relevant to long-

658   term CO_2 mineral trapping.

659

667   REFERENCES

668   (1)   Bruant, R. G., Jr.; Guswa, A. J.; Celia, M. A.; Peters, C. A. Safe storage of CO_2 in deep
669   saline aquifers. *Environ. Sci. Technol.* **2002**, *36*, 240A – 245A.

670   (2)   Pacala, S.; Socolow, R. Stabilization wedges: solving the climate problem for the next 50
671   years with current technologies. *Science* **2004**, *305*, 968–972.

672   (3)   Metz, B., Davidson, O., de Coninck, H., Loos, M., Meyer, L., Eds. *IPCC Special Report*
673   *on Carbon Dioxide Capture and Storage*; Cambridge University Press, 2005; p 430.

674   (4)   Bachu, S. CO_2 storage in geological media: Role, means, status and barriers to
675   deployment. *Prog. Energy Combust. Sci.* **2008**, *34*, 254–273.

676   (5)   Benson, S. M.; Cole, D. R. CO_2 sequestration in deep sedimentary formations. *Elements*
677   **2008**, *4*, 325–331.

678   (6)   Haszeldine, R. S. Carbon capture and storage: How green can black be. *Science* **2009**,
679   *325*, 1647–1652.

680   (7)   Smit, B.; Reimer, J. A.; Oldenburg, C. M.; Bourg, I. C. *Introduction to Carbon Capture*
681   *and Sequestration*; Imperial College Press, 2014.

682   (8)   Stauffer, P. H.; Keating, G. N.; Middleton, R. S.; Viswanathan, H. S.; Berchtold, K. A.;
683   Singh, R. P.; Pawar, R. J.; Mancino, A. Greening coal: Breakthroughs and challenges in
684   carbon capture and storage. *Environ. Sci. Technol.* **2011**, *45*, 8597–8604.

685   (9)   Rubin, E. S.; Zhai, H. The cost of carbon capture and storage for natural gas combined
686   cycle power plants. *Environ. Sci. Technol.* **2012**, *46*, 3076–3084.

687   (10)   Eccles, J. K.; Pratson, L.; Newell, R. G.; Jackson, R. B. Physical and economic potential
688   of geological CO_2 storage in saline aquifers. *Environ. Sci. Technol.* **2009**, *43*, 1962–1969.

689   (11)   Hovorka, S. D.; Benson, S. M.; Doughty, C.; Freifeld, B. M.; Sakurai, S.; Daley, T. M.;
690   Kharaka, Y. K.; Holtz, M. H.; Trautz, R. C.; Nance, H. S.; et al. Measuring permanence of
691   CO_2 storage in saline formations: the Frio experiment. *Environ. Geosci.* **2006**, *13*, 105–
692   121.

693   (12)   Chadwick, A.; Williams, G.; Delepine, N.; Clochard, V.; Labat, K.; Sturton, S.;
694   Buddensiek, M.-L.; Dillen, M.; Nickel, M.; Lima, A. L.; et al. Quantitative analysis of
695   time-lapse seismic monitoring data at the Sleipner CO_2 storage operation. *Lead. Edge*
696   **2010**, *29*, 170–177.

697   (13)   Michael, K.; Golab, A.; Shulakova, V.; Ennis-King, J.; Allinson, G.; Sharma, S.; Aiken,
698   T. Geological storage of CO_2 in saline aquifers—A review of the experience from existing
699   storage operations. *Int. J. Greenh. Gas Control* **2010**, *4*, 659–667.

700   (14)   Daley, T. M.; Ajo-Franklin, J. B.; Doughty, C. Constraining the reservoir model of an
701   injected CO_2 plume with crosswell CASSM at the Frio-II brine pilot. *Int. J. Greenh. Gas
702   Control* **2011**, *5*, 1022–1030.

703   (15)   Sato, K.; Mito, S.; Horie, T.; Ohkuma, H.; Saito, H.; Watanabe, J.; Yoshimura, T.
704   Monitoring and simulation studies for assessing macro- and meso-scale migration of CO_2
705   sequestered in an onshore aquifer: Experiences from the Nagaoka pilot site, Japan. *Int. J.
706   Greenh. Gas Control* **2011**, *5*, 125–137.

707   (16)   Underschultz, J.; Boreham, C.; Dance, T.; Stalker, L.; Freifeld, B.; Kirste, D.; Ennis-King,
708   J. CO_2 storage in a depleted gas field: An overview of the CO2CRC Otway Project and
709   initial results. *Int. J. Greenh. Gas Control* **2011**, *5*, 922–932.

710   (17)   Kharaka, Y. K.; Cole, D. R.; Thordsen, J. J.; Gans, K. D.; Thomas, R. B. Geochemical
711   monitoring for potential environmental impacts of geologic sequestration of CO_2. *Rev.
712   Mineral. Geochemistry* **2013**, *77*, 399–430.

713   (18)   Goodman, A.; Hakala, A.; Bromhal, G.; Deel, D.; Rodosta, T.; Frailey, S.; Small, M.;
714   Allen, D.; Romanov, V.; Fazio, J.; et al. U.S. DOE methodology for the development of
715   geologic storage potential for carbon dioxide at the national and regional scale. *Int. J.
716   Greenh. Gas Control* **2011**, *5*, 952–965.

717   (19)   Marieni, C.; Henstock, T. J.; Teagle, D. A. H. Geological storage of CO_2 within the
718   oceanic crust by gravitational trapping. *Geophys. Res. Lett.* **2013**, *40*, 6219–6224.

719   (20)   Zhang, S.; DePaolo, D. J.; Xu, T.; Zheng, L. Mineralization of carbon dioxide sequestered
720   in volcanogenic sandstone reservoir rocks. *Int. J. Greenh. Gas Control* **2013**, *18*, 315–328.

721   (21)   House, K. Z.; Schrag, D. P.; Harvey, C. F.; Lackner, K. S. Permanent carbon dioxide
722   storage in deep-sea sediments. *Proc. Natl. Acad. Sci. U. S. A.* **2006**, *103*, 12291–12295.

723   (22)   Espinoza, D. N.; Santamarina, J. C. P-wave monitoring of hydrate-bearing sand during
724   CH_4–CO_2 replacement. *Int. J. Greenh. Gas Control* **2011**, *5*, 1031–1038.

725   (23)   Juanes, R.; Spiteri, E. J.; Orr, F. M., Jr.; Blunt, M. J. Impact of relative permeability
726   hysteresis on geological CO_2 storage. *Water Resour. Res.* **2006**, *42*, W12418.

727   (24)   Doughty, C. Investigation of CO_2 plume behavior for a large-scale pilot test of geologic
728   carbon storage in a saline formation. *Transp. Porous Media* **2010**, *82*, 49–76.

729   (25)   Würdemann, H.; Möller, F.; Kühn, M.; Heidug, W.; Christensen, N. P.; Borm, G.;
730   Schilling, F. R.; the CO2SINK Group. CO2SINK—From site characterization and risk

731   assessment to monitoring and verification: One year of operational experience with the
732   field laboratory for CO_2 storage at Ketzin, Germany. *Int. J. Greenh. Gas Control* **2010**, *4*,
733   938–951.

734   (26)   Zhou, Q.; Birkholzer, J. T.; Mehnert, E.; Lin, Y.-F.; Zhang, K. Modeling basin- and
735   plume-scale processes of CO_2 storage for full-scale deployment. *Ground Water* **2010**, *48*,
736   494–514.

737   (27)   Cappa, F.; Rutqvist, J. Modeling of coupled deformation and permeability evolution
738   during fault reactivation induced by deep underground injection of CO_2. *Int. J. Greenh.*
739   *Gas Control* **2011**, *5*, 336–346.

740   (28)   Liu, F.; Lu, P.; Zhu, C.; Xiao, Y. Coupled reactive flow and transport modeling of CO_2
741   sequestration in the Mt. Simon sandstone formation, Midwest U.S.A. *Int. J. Greenh. Gas*
742   *Control* **2011**, *5*, 294–307.

743   (29)   Buscheck, T. A.; Sun, Y.; Chen, M.; Hao, Y.; Wolery, T. J.; Bourcier, W. L.; Court, B.;
744   Celia, M. A.; Friedmann, S. J.; Aines, R. D. Active CO_2 reservoir management for carbon
745   storage: Analysis of operational strategies to relieve pressure buildup and improve
746   injectivity. *Int. J. Greenh. Gas Control* **2012**, *6*, 230–245.

747   (30)   Noy, D. J. J.; Holloway, S.; Chadwick, R. A.; Williams, J. D. O.; Hannis, S. A.; Lahann,
748   R. W. Modelling large-scale carbon dioxide injection into the Bunter Sandstone in the UK
749   Southern North Sea. *Int. J. Greenh. Gas Control* **2012**, *9*, 220–233.

750   (31)   Olden, P.; Pickup, G.; Jin, M.; Mackay, E.; Hamilton, S.; Somerville, J.; Todd, A. Use of
751   rock mechanics laboratory data in geomechanical modelling to increase confidence in CO_2
752   geological storage. *Int. J. Greenh. Gas Control* **2012**, *11*, 304–315.

753   (32)   Cavanagh, A.; Rostron, B. High-resolution simulations of migration pathways and the
754   related potential well risk at the IEAGHG Weyburn–Midale CO_2 storage project. *Int. J.*
755   *Greenh. Gas Control* **2013**, *16S*, S15–S24.

756   (33)   Cavanagh, A. J.; Haszeldine, R. S. The Sleipner storage site: Capillary flow modeling of a
757   layered CO_2 plume requires fractured shale barriers within the Utsira Formation. *Int. J.*
758   *Greenh. Gas Control* **2014**, *21*, 101–112.

759   (34)   Huang, X.; Bandilla, K. W.; Celia, M. A.; Bachu, S. Basin-scale modeling of CO_2 storage
760   using models of varying complexity. *Int. J. Greenh. Gas Control* **2014**, *20*, 73–86.

761   (35)   Konstantinovskaya, E.; Rutqvist, J.; Malo, M. CO_2 storage and potential fault instability in
762   the St. Lawrence Lowlands sedimentary basin (Quebec, Canada): Insights from coupled
763   reservoir-geomechanical modeling. *Int. J. Greenh. Gas Control* **2014**, *22*, 88–110.

764   (36)   Sung, R.-T.; Li, M.-H.; Dong, J.-J.; Lin, A. T.-S.; Hsu, S.-K.; Wang, C.-Y.; Yang, C.-N.
765   Numerical assessment of CO_2 geological sequestration in sloping and layered

766   heterogeneous formations: A case study from Taiwan. *Int. J. Greenh. Gas Control* **2014**,
767   *20*, 168–179.

768   (37)   Nordbotten, J. M.; Flemisch, B.; Gasda, S. E.; Nilsen, H. M.; Fan, Y.; Pickup, G. E.;
769   Wiese, B.; Celia, M. A.; Dahle, H. K.; Eigestad, G. T.; et al. Uncertainties in practical
770   simulation of CO_2 storage. *Int. J. Greenh. Gas Control* **2012**, *9*, 234–242.

771   (38)   Mito, S.; Xue, Z.; Sato, T. Effect of formation water composition on predicting CO_2
772   behavior: A case study at the Nagaoka post-injection monitoring site. *Appl. Geochemistry*
773   **2013**, *30*, 33–40.

774   (39)   Rutqvist, J. The geomechanics of CO_2 storage in deep sedimentary formations. *Geotech.*
775   *Geol. Eng.* **2012**, *30*, 525–551.

776   (40)   Szulczewski, M. L.; MacMinn, C. W.; Herzog, H. J.; Juanes, R. Lifetime of carbon
777   capture and storage as a climate-change mitigation technology. *Proc. Natl. Acad. Sci. U.*
778   *S. A.* **2012**, *109*, 5185–5189.

779   (41)   Doughty, C. Modeling geologic storage of carbon dioxide: Comparison of non-hysteretic
780   and hysteretic characteristic curves. *Energy Convers. Manag.* **2007**, *48*, 1768–1781.

781   (42)   Xu, T.; Apps, J. A.; Pruess, K.; Yamamoto, H. Numerical modeling of injection and
782   mineral trapping of CO_2 with H_2S and SO_2 in a sandstone formation. *Chem. Geol.* **2007**,
783   *242*, 319–346.

784   (43)   Gaus, I.; Azaroual, M.; Czernichowski-Lauriol, I. Reactive transport modelling of the
785   impact of CO_2 injection on the clayey cap rock at Sleipner (North Sea). *Chem. Geol.* **2005**,
786   *217*, 319–337.

787   (44)   Pham, V. T. H.; Lu, P.; Aagaard, P.; Zhu, C.; Hellevang, H. On the potential of CO_2-
788   water-rock interactions for CO_2 storage using a modified kinetic model. *Int. J. Greenh.*
789   *Gas Control* **2011**, *5*, 1002–1015.

790   (45)   Zhang, M.; Bachu, S. Review of integrity of existing wells in relation to CO_2 geological
791   storage: What do we know? *Int. J. Greenh. Gas Control* **2011**, *5*, 826–840.

792   (46)   Gaus, I.; Audigane, P.; André, L.; Lions, J.; Jacquemet, N.; Durst, P.; Czernichowski-
793   Lauriol, I.; Azaroual, M. Geochemical and solute transport modelling for CO_2 storage,
794   what to expect from it? *Int. J. Greenh. Gas Control* **2008**, *2*, 605–625.

795   (47)   Vilarrasa, V.; Silva, O.; Carrera, J.; Olivella, S. Liquid CO_2 injection for geological
796   storage in deep saline aquifers. *Int. J. Greenh. Gas Control* **2013**, *14*, 84–96.

797   (48)   Li, B.; Tchelepi, H. A.; Benson, S. M. Influence of capillary-pressure models on CO_2
798   solubility trapping. *Adv. Water Resour.* **2013**, *62*, 488–498.

799   (49)   Saraji, S.; Piri, M.; Goual, L. The effects of SO_2 contamination, brine salinity, pressure,
800   and temperature on dynamic contact angles and interfacial tension of supercritical
801   CO_2/brine/quartz systems. *Int. J. Greenh. Gas Control* **2014**, *28*, 147–155.

802   (50)   Berg, S.; Ott, H. Stability of CO_2–brine immiscible displacement. *Int. J. Greenh. Gas
803   Control* **2012**, *11*, 188–203.

804   (51)   Pini, R.; Krevor, S. C. M.; Benson, S. M. Capillary pressure and heterogeneity for the
805   CO_2/water system in sandstone rocks at reservoir conditions. *Adv. Water Resour.* **2012**,
806   *38*, 48–59.

807   (52)   Oldenburg, C. M.; Webb, S. W.; Pruess, K.; Moridis, G. J. Mixing of stably stratified
808   gases in subsurface reservoirs: A comparison of diffusion models. *Transp. Porous Media*
809   **2004**, *54*, 323–334.

810   (53)   Mathias, S. A.; Gluyas, J. G.; González Martínez de Miguel, G. J.; Bryant, S. L.; Wilson,
811   D. On relative permeability data uncertainty and CO_2 injectivity estimation for brine
812   aquifers. *Int. J. Greenh. Gas Control* **2013**, *12*, 200–212.

813   (54)   Sbai, M. A.; Azaroual, M. Numerical modeling of formation damage by two-phase
814   particulate transport processes during CO_2 injection in deep heterogeneous porous media.
815   *Adv. Water Resour.* **2011**, *34*, 62–82.

816   (55)   Bodnar, R. J.; Steele-MacInnis, M.; Capobianco, R. M.; Rimstidt, J. D.; Dilmore, R.;
817   Goodman, A.; Guthrie, G. PVTX properties of H_2O-CO_2-"salt" at PTX conditions
818   applicable to carbon sequestration in saline formations. *Rev. Mineral. Geochemistry* **2013**,
819   *77*, 123–152.

820   (56)   Carroll, S. A.; Keating, E.; Mansoor, K.; Dai, Z.; Sun, Y.; Trainor-Guitton, W.; Brown,
821   C.; Bacon, D. Key factors for determining groundwater impacts due to leakage from
822   geologic carbon sequestration reservoirs. *Int. J. Greenh. Gas Control* **2014**, *29*, 153–168.

823   (57)   Burant, A.; Lowry, G. V; Karamalidis, A. K. Partitioning behavior of organic
824   contaminants in carbon storage environments: A critical review. *Environ. Sci. Technol.*
825   **2012**, *47*, 37–54.

826   (58)   Ambrose, W. A.; Lakshminarasimhan, S.; Holtz, M. H.; Núñez-López, V.; Hovorka, S.
827   D.; Duncan, I. Geologic factors controlling CO_2 storage capacity and permanence: case
828   studies based on experience with heterogeneity in oil and gas reservoirs applied to CO_2
829   storage. *Environ. Geol.* **2008**, *54*, 1619–1633.

830   (59)   Saadatpoor, E.; Bryant, S. L.; Sepehrnoori, K. New trapping mechanism in carbon
831   sequestration. *Transp. Porous Media* **2010**, *82*, 3–17.

832   (60)   Deng, H.; Stauffer, P. H.; Dai, Z.; Jiao, Z.; Surdam, R. C. Simulation of industrial-scale
833   CO_2 storage: Multi-scale heterogeneity and its impacts on storage capacity, injectivity and
834   leakage. *Int. J. Greenh. Gas Control* **2012**, *10*, 397–418.

835   (61)   Birkholzer, J. T.; Zhou, Q.; Tsang, C.-F. Large-scale impact of CO_2 storage in deep saline
836   aquifers: A sensitivity study on pressure response in stratified systems. *Int. J. Greenh. Gas
837   Control* **2009**, *3*, 181–194.

838   (62)   Bretan, P.; Yielding, G.; Mathiassen, O. M.; Thorsnes, T. Fault-seal analysis for CO_2
839   storage: an example from the Troll area, Norwegian Continental Shelf. *Pet. Geosci.* **2011**,
840   *17*, 181–192.

841   (63)   Zoback, M. D.; Gorelick, S. M. Earthquake triggering and large-scale geologic storage of
842   carbon dioxide. *Proc. Natl. Acad. Sci. U. S. A.* **2012**, *109*, 10164–10168.

843   (64)   Amann-Hildenbrand, A.; Bertier, P.; Busch, A.; Krooss, B. M. Experimental investigation
844   of the sealing capacity of generic clay-rich caprocks. *Int. J. Greenh. Gas Control* **2013**,
845   *19*, 620–641.

846   (65)   Busch, A.; Amann-Hildenbrand, A. Predicting capillarity of mudrocks. *Mar. Pet. Geol.*
847   **2013**, *45*, 208–223.

848   (66)   Aydin, A. Fractures, faults, and hydrocarbon entrapment, migration and flow. *Mar. Pet.
849   Geol.* **2000**, *17*, 797–814.

850   (67)   Boisson, J.-Y.; Bertrand, L.; Heitz, J.-F.; Moreau-Le Golvan, Y. In situ and laboratory
851   investigations of fluid flow through an argillaceous formation at different scales of space
852   and time, Tournemire tunnel, southern France. *Hydrogeol. J.* **2001**, *9*, 108–123.

853   (68)   Cosgrove, J. W. Hydraulic fracturing during the formation and deformation of a basin: A
854   factor in the dewatering of low-permeability sediments. *Am. Assoc. Pet. Geol. Bull.* **2001**,
855   *85*, 737–748.

856   (69)   Aplin, A. C.; Larter, S. R. Fluid flow, pore pressure, wettability, and leakage in mudstone
857   cap rocks. In *Evaluating fault and cap rock seals: AAPG Hedberg Series, no. 2*; Boult, P.,
858   Kadli, J., Eds.; The American Association of Petroleum Geologists, 2005; pp 1–12.

859   (70)   Bachu, S.; Bennion, D. B. Experimental assessment of brine and/or CO_2 leakage through
860   well cements at reservoir conditions. *Int. J. Greenh. Gas Control* **2009**, *3*, 494–501.

861   (71)   Crow, W.; Carey, J. W.; Gasda, S.; Williams, D. B.; Celia, M. Wellbore integrity analysis
862   of a natural CO_2 producer. *Int. J. Greenh. Gas Control* **2010**, *4*, 186–197.

863   (72)   Celia, M. A.; Nordbotten, J. M.; Court, B.; Dobossy, M.; Bachu, S. Field-scale application
864   of a semi-analytical model for estimation of CO_2 and brine leakage along old wells. *Int. J.
865   Greenh. Gas Control* **2011**, *5*, 257–269.

866   (73)   Mazurek, M.; Alt-Epping, P.; Bath, A.; Gimmi, T.; Waber, H. N.; Buschaert, S.; De
867   Cannière, P.; De Craen, M.; Gautschi, A.; Savoye, S.; et al. Natural tracer profiles across
868   argillaceous formations. *Appl. Geochemistry* **2011**, *26*, 1035–1064.

869   (74)   Carey, J. W. Geochemistry of wellbore integrity in CO_2 sequestration: Portland cement-
870   steel-brine-CO_2 interactions. *Rev. Mineral. Geochemistry* **2013**, *77*, 505–539.

871   (75)   Song, J.; Zhang, D. Comprehensive review of caprock-sealing mechanisms for geologic
872   carbon sequestration. *Environ. Sci. Technol.* **2013**, *47*, 9–22.

873   (76)   Griffith, C. A.; Dzombak, D. A.; Lowry, G. V. Physical and chemical characteristics of
874   potential seal strata in regions considered for demonstrating geological saline CO_2
875   sequestration. *Environ. Earth Sci.* **2011**, *64*, 925–948.

876   (77)   Dewhurst, D. N.; Yang, Y.; Aplin, A. C. Permeability and fluid flow in natural mudstones.
877   *Geol. Soc. London, Spec. Publ.* **1999**, *158*, 23–43.

878   (78)   Best, M. E.; Katsube, T. J. Shale permeability and its significance in hydrocarbon
879   exploration. *Lead. Edge* **1995**, *14* (March), 165–170.

880   (79)   Bickle, M.; Kampman, N.; Wigley, M. Natural analogues. *Rev. Mineral. Geochemistry*
881   **2013**, *77*, 15–71.

882   (80)   Yang, Y.; Aplin, A. C. A permeability–porosity relationship for mudstones. *Mar. Pet.*
883   *Geol.* **2010**, *27*, 1692–1697.

884   (81)   Grunau, H. R. A worldwide look at the cap-rock problem. *J. Pet. Geol.* **1987**, *10*, 245–
885   266.

886   (82)   Gautschi, A. Hydrogeology of a fractured shale (Opalinus Clay): Implications for deep
887   geological disposal of radioactive wastes. *Hydrogeol. J.* **2001**, *9*, 97–107.

888   (83)   Croisé, J.; Schlickenrieder, L.; Marschall, P.; Boisson, J. Y.; Vogel, P.; Yamamoto, S.
889   Hydrogeological investigations in a low permeability claystone formation: the Mont Terri
890   Rock Laboratory. *Phys. Chem. Earth* **2004**, *29*, 3–15.

891   (84)   Mazurek, M.; Alt-Epping, P.; Bath, A.; Gimmi, T.; Waber, H. N. *Natural tracer profiles*
892   *across argillaceous formations: The CLAYTRAC Project*; Nuclear Energy Agency,
893   Organisation for Economic Co-Operation and Development: Paris, 2009.

894   (85)   Gutierrez, M.; Øino, L. E.; Nygård, R. Stress-dependent permeability of a de-mineralised
895   fracture in shale. *Mar. Pet. Geol.* **2000**, *17*, 895–907.

896   (86)   Bock, H.; Dehandschutter, B.; Martin, C. D.; Mazurek, M.; de Haller, A.; Skoczylas, F.;
897   Davy, C. *Self-sealing of fractures in argillaceous formations in the context of geological*

898   *disposal of radioactive waste: Review and synthesis*; Nuclear Energy Agency,
899   Organisation for Economic Co-Operation and Development: Paris, 2010.

900 (87) Neuzil, C. E. How permeable are clays and shales? *Water Resour. Res.* **1994**, *30*, 145–
901   150.

902 (88) Neuzil, C. E. Can shale safely host U.S. nuclear waste? *EOS, Trans. Am. Geophys. Union*
903   **2013**, *94*, 261–268.

904 (89) Mitchell, T. M.; Faulkner, D. R. Towards quantifying the matrix permeability of fault
905   damage zones in low porosity rocks. *Earth Planet. Sci. Lett.* **2012**, *339-340*, 24–31.

906 (90) Caine, J. S.; Evans, J. P.; Forster, C. B. Fault zone architecture and permeability structure.
907   *Geology* **1996**, *24*, 1025–1028.

908 (91) Motellier, S.; Devol-Brown, I.; Savoye, S.; Thoby, D.; Alberto, J.-C. Evaluation of
909   tritiated water diffusion through the Toarcian clayey formation of the Tournemire
910   experimental site (France). *J. Contam. Hydrol.* **2007**, *94*, 99–108.

911 (92) Wollenweber, J.; Alles, S.; Busch, A.; Krooss, B. M.; Stanjek, H.; Littke, R. Experimental
912   investigation of the CO_2 sealing efficiency of caprocks. *Int. J. Greenh. Gas Control* **2010**,
913   *4*, 231–241.

914 (93) May, F. Alteration of wall rocks by CO_2-rich water ascending in fault zones: Natural
915   analogues for reactions induced by CO_2 migrating along faults in siliciclastic reservoir and
916   cap rocks. *Oil Gas Sci. Technol.* **2005**, *60*, 19–32.

917 (94) Andreani, M.; Gouze, P.; Luquot, L.; Jouanna, P. Changes in seal capacity of fractured
918   claystone caprocks induced by dissolved and gaseous CO_2 seepage. *Geophys. Res. Lett.*
919   **2008**, *35*, L14404.

920 (95) Bildstein, O.; Kervévan, C.; Lagneau, V.; Delaplace, P.; Crédoz, A.; Audigane, P.;
921   Perfetti, E.; Jacquemet, N.; Jullien, M. Integrative modeling of caprock integrity in the
922   context of CO_2 storage: Evolution of transport and geochemical properties and impact on
923   performance and safety assessment. *Oil Gas Sci. Technol.* **2010**, *65*, 485–502.

924 (96) Ellis, B. R.; Bromhal, G. S.; McIntyre, D. L.; Peters, C. A. Changes in caprock integrity
925   due to vertical migration of CO_2-enriched brine. *Energy Procedia* **2011**, *4*, 5327–5334.

926 (97) Wibberley, C. A. J.; Yielding, G.; Di Toro, G. Recent advances in the understanding of
927   fault zone internal structure: a review. *Geol. Soc. London, Spec. Publ.* **2008**, *299*, 5–33.

928 (98) Manzocchi, T.; Childs, C.; Walsh, J. J. Faults and fault properties in hydrocarbon flow
929   models. *Geofluids* **2010**, *10*, 94–113.

930   (99)   Crawford, B. R.; Faulkner, D. R.; Rutter, E. H. Strength, porosity, and permeability
931   development during hydrostatic and shear loading of synthetic quartz-clay fault gouge. *J.*
932   *Geophys. Res.* **2008**, *113*, B03207.

933   (100) Manzocchi, T.; Walsh, J. J.; Nell, P.; Yielding, G. Fault transmissibility multipliers for
934   flow simulation models. *Pet. Geosci.* **1999**, *5*, 53–63.

935   (101) Yielding, G. Using probabilistic shale smear modelling to relate SGR predictions of
936   column height to fault-zone heterogeneity. *Pet. Geosci.* **2012**, *18*, 33–42.

937   (102) Dewhurst, D. N.; Hennig, A. L. Geomechanical properties related to top seal leakage in
938   the Carnarvon Basin, Northwest Shelf, Australia. *Pet. Geosci.* **2003**, *9*, 255–263.

939   (103) Pan, P.-Z.; Rutqvist, J.; Feng, X.-T.; Yan, F. Modeling of caprock discontinuous
940   fracturing during CO_2 injection into a deep brine aquifer. *Int. J. Greenh. Gas Control*
941   **2013**, *19*, 559–575.

942   (104) Sibson, R. H. A note on fault reactivation. *J. Struct. Geol.* **1985**, *7*, 751–754.

943   (105) Byerlee, J. Friction of rocks. *Pure Appl. Geophys.* **1978**, *116*, 615–626.

944   (106) Morrow, C. A.; Shi, L. Q.; Byerlee, J. D. Permeability of fault gouge under confining
945   pressure and shear stress. *J. Geophys. Res.* **1984**, *89*, 3193-3200.

946   (107) Ingram, G. M.; Urai, J. L. Top-seal leakage through faults and fractures: the role of
947   mudrock properties. *Geol. Soc. London, Spec. Publ.* **1999**, *158*, 125–135.

948   (108) Schleicher, A. M.; Hofmann, H.; van der Pluijm, B. A. Constraining clay hydration state
949   and its role in active fault systems. *Geochem. Geophys. Geosyst.* **2013**, *14*, 1039–1052.

950   (109) Burland, J. B. On the compressibility and shear strength of natural clays. *Géotechnique*
951   **1990**, *40*, 329–378.

952   (110) Mutschler, T.; Triantafyllidis, T.; Balthasar, K. Geotechnical investigations of cap rocks
953   above CO_2-reservoirs. *Energy Procedia* **2009**, *1*, 3375–3382.

954   (111) Elkhoury, J. E.; Ameli, P.; Detwiler, R. L. Dissolution and deformation in fractured
955   carbonates caused by flow of CO_2-rich brine under reservoir conditions. *Int. J. Greenh.*
956   *Gas Control* **2013**, *16S*, S203–S215.

957   (112) Young, A.; Low, P. F.; McLatchie, A. S. Permeability studies of argillaceous rocks. *J.*
958   *Geophys. Res.* **1964**, *69*, 4237–4245.

959   (113) Nadeau, P. H. An experimental study of the effects of diagenetic clay minerals on
960   reservoir sands. *Clays Clay Miner.* **1998**, *46*, 18–26.

961   (114) Gouze, P.; Luquot, L. X-ray microtomography characterization of porosity, permeability
962   and reactive surface changes during dissolution. *J. Contam. Hydrol.* **2011**, *120-121*, 45–
963   55.

964   (115) Fitts, J. P.; Peters, C. A. Caprock fracture dissolution and CO_2 leakage. *Rev. Mineral.*
965   *Geochemistry* **2013**, *77*, 459–479.

966   (116) Steefel, C. I.; Molins, S.; Trebotich, D. Pore scale processes associated with subsurface
967   CO_2 injection and sequestration. *Rev. Mineral. Geochemistry* **2013**, *77*, 259–303.

968   (117) Bacci, G.; Korre, A.; Durucan, S. Experimental investigation into salt precipitation during
969   CO_2 injection in saline aquifers. *Energy Procedia* **2011**, *4*, 4450–4456.

970   (118) Yang, Y.; Aplin, A. C. Permeability and petrophysical properties of 30 natural mudstones.
971   *J. Geophys. Res.* **2007**, *112*, B03206.

972   (119) Mondol, N. H.; Bjørlykke, K.; Jahren, J. Experimental compaction of clays: relationship
973   between permeability and petrophysical properties in mudstones. *Pet. Geosci.* **2008**, *14*,
974   319–337.

975   (120) Mesri, G.; Olson, R. E. Mechanisms controlling the permeability of clays. *Clays Clay*
976   *Miner.* **1971**, *19*, 151–158.

977   (121) Vasseur, G.; Djeran-Maigre, I.; Grunberger, D.; Rousset, G.; Tessier, D.; Velde, B.
978   Evolution of structural and physical parameters of clays during experimental compaction.
979   *Mar. Pet. Geol.* **1995**, *12*, 941–954.

980   (122) Yang, Y.; Aplin, A. C. Definition and practical application of mudstone porosity-effective
981   stress relationships. *Pet. Geosci.* **2004**, *10*, 153–162.

982   (123) Reece, J. S.; Flemings, P. B.; Dugan, B.; Long, H.; Germaine, J. T. Permeability-porosity
983   relationships of shallow mudstones in the Ursa Basin, northern deepwater Gulf of Mexico.
984   *J. Geophys. Res.* **2012**, *117*, B12102.

985   (124) Tessier, D.; Lajudie, A.; Petit, J.-C. Relation between the macroscopic behavior of clays
986   and their microstructural properties. *Appl. Geochemistry* **1992**, *7* (Supl. Issue 1), 151–161.

987   (125) Sherwood, J. D. Ionic transport in swelling shale. *Adv. Colloid Interface Sci.* **1995**, *61*,
988   51–64.

989   (126) Anderson, R. L.; Ratcliffe, I.; Greenwell, H. C.; Williams, P. A.; Cliffe, S.; Coveney, P.
990   V. Clay swelling — A challenge in the oilfield. *Earth-Science Rev.* **2010**, *98*, 201–216.

991   (127) Dusseault, M. B. Geomechanical challenges in petroleum reservoir exploration. *KSCE J.*
992   *Civ. Eng.* **2011**, *15*, 669–678.

993   (128) Bruand, A.; Tessier, D. Water retention properties of the clay in soils developed on clayey
994   sediments: significance of parent material and soil history. *Eur. J. Soil Sci.* **2000**, *51*, 679–
995   688.

996   (129) Fitts, T. G.; Brown, K. M. Stress-induced smectite dehydration: ramifications for patterns
997   of freshening and fluid expulsion in the N. Barbados accretionary wedge. *Earth Planet.*
998   *Sci. Lett.* **1999**, *172*, 179–197.

999   (130) Dewhurst, D. N.; Siggins, A. F. Impact of fabric, microcracks and stress field on shale
1000   anisotropy. *Geophys. J. Int.* **2006**, *165*, 135–148.

1001 (131) Heath, J. E.; Dewers, T. A.; McPherson, B. J. O. L.; Petrusak, R.; Chidsey, T. C., Jr.;
1002   Rinehart, A. J.; Mozley, P. S. Pore networks in continental and marine mudstones:
1003   Characteristics and controls on sealing behavior. *Geosphere* **2011**, *7*, 429–454.

1004 (132) Mbia, E. N.; Frykman, P.; Nielsen, C. M.; Fabricius, I. L.; Pickup, G. E.; Bernstone, C.
1005   Caprock compressibility and permeability and the consequences for pressure development
1006   in CO_2 storage sites. *Int. J. Greenh. Gas Control* **2014**, *22*, 139–153.

1007 (133) Katsube, T. J.; Mudford, B. S.; Best, M. E. Petrophysical characteristics of shales from the
1008   Scotian shelf. *Geophysics* **1991**, *56*, 1681–1689.

1009 (134) Josh, M.; Esteban, L.; Delle Piane, C.; Sarout, J.; Dewhurst, D. N.; Clennell, M. B.
1010   Laboratory characterisation of shale properties. *J. Pet. Sci. Eng.* **2012**, *88-89*, 107–124.

1011 (135) Skurtveit, E.; Aker, E.; Soldal, M.; Angeli, M.; Wang, Z. Experimental investigation of
1012 CO_2 breakthrough and flow mechanisms in shale. *Pet. Geosci.* **2012**, *18*, 3–15.

1013 (136) Keller, L. M.; Schuetz, P.; Erni, R.; Rossell, M. D.; Lucas, F.; Gasser, P.; Holzer, L.
1014   Characterization of multi-scale microstructural features in Opalinus Clay. *Microporous*
1015   *Mesoporous Mater.* **2013**, *170*, 83–94.

1016 (137) Curtis, M. E.; Sondergeld, C. H.; Ambrose, R. J.; Rai, C. S. Microstructural investigation
1017   of gas shales in two and three dimensions using nanometer-scale resolution imaging. *Am.*
1018   *Assoc. Pet. Geol. Bull.* **2012**, *96*, 665–677.

1019 (138) Nelson, P. H. Pore-throat sizes in sandstones, tight sandstones, and shales. *Am. Assoc. Pet.*
1020   *Geol. Bull.* **2009**, *93*, 329–340.

1021 (139) Altmann, S.; Tournassat, C.; Goutelard, F.; Parneix, J.-C.; Gimmi, T.; Maes, N. Diffusion-
1022   driven transport in clayrock formations. *Appl. Geochemistry* **2012**, *27*, 463–478.

1023 (140) Schlömer, S.; Krooss, B. M. Experimental characterisation of the hydrocarbon sealing
1024   efficiency of cap rocks. *Mar. Pet. Geol.* **1997**, *14*, 565–580.

1025 (141) Yven, B.; Sammartino, S.; Geraud, Y.; Homand, F.; Villieras, F. Mineralogy, texture and
1026   porosity of Callovo-Oxfordian argillites of the Meuse/Haute-Marne region (eastern Paris
1027   Basin). *Mém. Soc. Géol. Fr.* **2007**, *178*, 73–90.

1028 (142) Hildenbrand, A.; Schlömer, S.; Krooss, B. M.; Littke, R. Gas breakthrough experiments in
1029   pelitic rocks: comparative study with N_2, CO_2, and CH_4. *Geofluids* **2004**, *4*, 61–80.

1030 (143) Ruppert, L. F.; Sakurovs, R.; Blach, T. P.; He, L.; Melnichenko, Y. B.; Mildner, D. F. R.;
1031   Alcantar-Lopez, L. A USANS/SANS study of the accessibility of pores in the Barnett
1032   shale to methane and water. *Energy & Fuels* **2013**, *27*, 772–779.

1033 (144) Swift, A. M.; Anovitz, L. M.; Sheets, J. M.; Cole, D. R.; Welch, S. A.; Rother, G.
1034   Relationship between mineralogy and porosity in seals relevant to geologic CO_2
1035   sequestration. *Environ. Geosci.* **2014**, *21*, 39–57.

1036 (145) Gu, X.; Cole, D. R.; Rother, G.; Mildner, D. F. R.; Brantley, S. L. Pores in Marcellus
1037   shale: A neutron scattering and FIB-SEM study. *Energy & Fuels* **2015**, *29*, 1295–1308.

1038 (146) Bryant, W. R.; Hottman, W.; Trabant, P. Permeability of unconsolidated and consolidated
1039   marine sediments, Gulf of Mexico. *Mar. Geotechnol.* **1975**, *1*, 1–14.

1040 (147) Bennett, R. H.; Fischer, K. M.; Lavoie, D. L.; Bryant, W. R.; Rezak, R. Porometry and
1041   fabric of marine clay and carbonate sediments: Determinants of permeability. *Mar. Geol.*
1042   **1989**, *89*, 127–152.

1043 (148) Kwon, O.; Kronenberg, A. K.; Gangi, A. F. Permeability of Wilcox shale and its effective
1044   pressure law. *J. Geophys. Res.* **2001**, *106*, 19339–19353.

1045 (149) Kwon, O.; Kronenberg, A. K.; Gangi, A. F.; Johnson, B.; Herbert, B. E. Permeability of
1046   illite-bearing shale: 1. Anisotropy and effects of clay content and loading. *J. Geophys.*
1047   *Res.* **2004**, *109*, B10205.

1048 (150) Djéran-Maigre, I.; Tessier, D.; Grunberger, D.; Velde, B.; Vasseur, G. Evolution of
1049   microstructures and of macroscopic properties of some clays during experimental
1050   compaction. *Mar. Pet. Geol.* **1998**, *15*, 109–128.

1051 (151) Zhang, J.; Scherer, G. W. Permeability of shale by the beam-bending method. *Int. J. Rock*
1052   *Mech. Min. Sci.* **2012**, *53*, 179–191.

1053 (152) Constantin, J.; Peyaud, J. B.; Vergély, P.; Pagel, M.; Cabrera, J. Evolution of the structural
1054   fault permeability in argillaceous rocks in a polyphased tectonic context. *Phys. Chem.*
1055   *Earth* **2004**, *29*, 25–41.

1056 (153) Wittebroodt, C.; Savoye, S.; Frasca, B.; Gouze, P.; Michelot, J.-L. Diffusion of HTO,
1057 $^{36}Cl^-$ and $^{125}I^-$ in Upper Toarcian argillite samples from Tournemire: Effects of initial
1058   iodide concentration and ionic strength. *Appl. Geochemistry* **2012**, *27*, 1432–1441.

1059   (154) Gaucher, E.; Robelin, C.; Matray, J. M.; Négrel, G.; Gros, Y.; Heitz, J. F.; Vinsot, A.;
1060   Rebours, H.; Cassagnabère, A.; Bouchet, A. ANDRA underground research laboratory:
1061   interpretation of the mineralogical and geochemical data acquired in the Callovian–
1062   Oxfordian formation by investigative drilling. *Phys. Chem. Earth* **2004**, *29*, 55–77.

1063   (155) Billiotte, J.; Yang, D.; Su, K. Experimental study on gas permeability of mudstones. *Phys.*
1064   *Chem. Earth* **2008**, *33*, S231–S236.

1065   (156) Savoye, S.; Goutelard, F.; Beaucaire, C.; Charles, Y.; Fayette, A.; Herbette, M.; Larabi,
1066   Y.; Coelho, D. Effect of temperature on the containment properties of argillaceous rocks:
1067   The case study of Callovo-Oxfordian claystones. *J. Contam. Hydrol.* **2011**, *125*, 102–112.

1068   (157) Melkior, T.; Yahiaoui, S.; Thoby, D.; Motellier, S.; Barthès, V. Diffusion coefficients of
1069   alkaline cations in Bure mudrock. **2007**, *32*, 453–462.

1070   (158) Descostes, M.; Blin, V.; Bazer-Bachi, F.; Meier, P.; Grenut, B.; Radwan, J.; Schlegel, M.
1071   L.; Buschaert, S.; Coelho, D.; Tevissen, E. Diffusion of anionic species in Callovo-
1072   Oxfordian argillites and Oxfordian limestones (Meuse/Haute–Marne, France). *Appl.*
1073   *Geochemistry* **2008**, *23*, 655–677.

1074   (159) Escoffier, S.; Homand, F.; Giraud, A.; Hoteit, N.; Su, K. Under stress permeability
1075   determination of the Meuse/Haute-Marne mudstone. *Eng. Geol.* **2005**, *81*, 329–340.

1076   (160) Marschall, P.; Horseman, S.; Gimmi, T. Characterisation of gas transport properties of the
1077   Opalinus Clay, a potential host rock formation for radioactive waste disposal. *Oil Gas Sci.*
1078   *Technol.* **2005**, *60*, 121–139.

1079   (161) Van Loon, L. R.; Müller, W.; Iijima, K. Activation energies of the self-diffusion of HTO,
1080 $^{22}Na^+$ and $^{36}Cl^-$ in a highly compacted argillaceous rock (Opalinus Clay). *Appl.*
1081   *Geochemistry* **2005**, *20*, 961–972.

1082   (162) Neuzil, C. E.; Provost, A. M. Recent experimental data may point to a greater role for
1083   osmotic pressures in the subsurface. *Water Resour. Res.* **2009**, *45*, W03410.

1084   (163) Wersin, P.; Van Loon, L. R.; Soler, J. M.; Yllera, A.; Eikenberg, J.; Gimmi, T.; Hernán,
1085   P.; Boisson, J.-Y. Long-term diffusion experiment at Mont Terri: first results from field
1086   and laboratory data. *Appl. Clay Sci.* **2004**, *26*, 123–135.

1087   (164) Appelo, C. A. J.; Van Loon, L. R.; Wersin, P. Multicomponent diffusion of a suite of
1088   tracers (HTO, Cl, Br, I, Na, Sr, Cs) in a single sample of Opalinus Clay. *Geochim.*
1089   *Cosmochim. Acta* **2010**, *74*, 1201–1219.

1090   (165) Förster, A.; Giese, R.; Juhlin, C.; Norden, B.; Springer, N.; the CO_2SINK Group. The
1091   geology of the CO_2SINK site: From regional scale to laboratory scale. *Energy Procedia*
1092   **2009**, *1*, 2911–2918.

1093   (166) Förster, A.; Norden, B.; Zinck-Jørgensen, K.; Frykman, P.; Kulenkampff, J.;
1094   Spangenberg, E.; Erzinger, J.; Zimmer, M.; Kopp, J.; Borm, G.; et al. Baseline
1095   characterization of the CO$_2$SINK geological storage site at Ketzin, Germany. *Environ.*
1096   *Geosci.* **2006**, *13*, 145–161.

1097   (167) Harrington, J. F.; Noy, D. J.; Horseman, S. T.; Birchall, D. J.; Chadwick, R. A. Laboratory
1098   study of gas and water flow in the Nordland Shale. In *Carbon Dioxide Sequestration in*
1099   *Geological Media—State of the Science*; Grobe, M., Pashin, J. C., Dodge, R. L., Eds.;
1100   American Association of Petroleum Geologists, 2009; pp 521–543.

1101   (168) Pillitteri, A.; Cerasi, P.; Stavrum, J.; Zweigel, P.; Bøe, R. *Rock mechanical tests of shale*
1102   *samples from the cap rock of the Utsira Sand in well 15/9-A11*; Report No.
1103   33.5324.00/06/03, SINTEF Petroleum Research, Trondheim, 2003.

1104   (169) Angeli, M.; Soldal, M.; Skurtveit, E.; Aker, E. Experimental percolation of supercritical
1105   CO2 through a caprock. *Energy Procedia* **2009**, *1*, 3351–3358.

1106   (170) Nadeau, P. H.; Peacor, D. R.; Yan, J.; Hillier, S. I-S precipitation in pore space as the
1107   cause of geopressuring in Mesozoic mudstones, Egersund Basin, Norwegian continental
1108   shelf. *Am. Mineral.* **2002**, *87*, 1580–1589.

1109   (171) Harrington, J. F.; Horseman, S. T. Gas transport properties of clays and mudrocks. *Geol.*
1110   *Soc. London, Spec. Publ.* **1999**, *158*, 107–124.

1111   (172) Nygård, R.; Gutierrez, M.; Høeg, K.; Bjørlykke, K. Influence of burial history on
1112   microstructure and compaction behaviour of Kimmeridge clay. *Pet. Geosci.* **2004**, *10*,
1113   259–270.

1114   (173) Busch, A.; Alles, S.; Gensterblum, Y.; Prinz, D.; Dewhurst, D. N.; Raven, M. D.; Stanjek,
1115   H.; Krooss, B. M. Carbon dioxide storage potential of shales. *Int. J. Greenh. Gas Control*
1116   **2008**, *2*, 297–308.

1117   (174) Dewhurst, D. N.; Jones, R. M.; Raven, M. D. Microstructural and petrophysical
1118   characterization of Muderong Shale: application to top seal risking. *Pet. Geosci.* **2002**, *8*
1119   (4), 371–383.

1120   (175) Nuccio, V. F.; Condon, S. M. *Burial and thermal history of the Paradox Basin, Utah and*
1121   *Colorado, and petroleum potential of the Middle Pennsylvanian Paradox Formation*;
1122   Bulletin 2000-O, U.S. Geological Survey, Washington, 1996.

1123   (176) Bereskin, S. R.; McLennan, J. *Hydrocarbon potential of Pennsylvanian black shale*
1124   *reservoirs, Paradox Basin, southeastern Utah*; Open-File Report 534, Utah Geological
1125   Survey, Salt Lake City, 2008.

1126　(177) Heath, J. E.; Dewers, T. A.; McPherson, B. J. O. L.; Nemer, M. B.; Kotula, P. G. Pore-
1127　　　　lining phases and capillary breakthrough pressure of mudstone caprocks: Sealing
1128　　　　efficiency of geologic CO_2 storage sites. *Int. J. Greenh. Gas Control* **2012**, *11*, 204–220.

1129　(178) Lu, J.; Milliken, K.; Reed, R. M.; Hovorka, S. Diagenesis and sealing capacity of the
1130　　　　middle Tuscaloosa mudstone at the Cranfield carbon dioxide injection site, Mississippi.
1131　　　　*Environ. Geosci.* **2011**, *18*, 35–53.

1132　(179) Pashin, J. C.; Kopaska-Merkel, D. C.; Arnold, A. C.; McIntyre, M. R. *Geological*
1133　　　　*foundation for production of natural gas from diverse shale formations*; Open File Report
1134　　　　1110, Geological Survey of Alabama, Tuscaloosa, 2011.

1135　(180) Tachi, Y.; Yotsuji, K.; Seida, Y.; Yui, M. Diffusion and sorption of Cs^+, I^- and HTO in
1136　　　　samples of the argillaceous Wakkanai Formation from the Horonobe URL, Japan: Clay-
1137　　　　based modeling approach. *Geochim. Cosmochim. Acta* **2011**, *75*, 6742–6759.

1138　(181) Takeda, M.; Hiratsuka, T.; Manaka, M.; Finsterle, S.; Ito, K. Experimental examination of
1139　　　　the relationships among chemico-osmotic, hydraulic, and diffusion parameters of
1140　　　　Wakkanai mudstones. *J. Geophys. Res. Solid Earth* **2014**, *119*, 010421.

1141　(182) Clarkson, C. R.; Solano, N.; Bustin, R. M.; Bustin, A. M. M.; Chalmers, G. R. L.; He, L.;
1142　　　　Melnichenko, Y. B. Pore structure characterization of North American shale gas reservoirs
1143　　　　using USANS/SANS, gas adsorption, and mercury intrusion. *Fuel* **2013**, *103*, 606–616.

1144　(183) Ghanizadeh, A.; Bhowmik, S.; Haeri-Ardakani, O.; Sanei, H.; Clarkson, C. R. A
1145　　　　comparison of shale permeability coefficients derived using multiple non-steady-state
1146　　　　measurement techniques: Examples from the Duvernay Formation, Alberta (Canada).
1147　　　　*Fuel* **2015**, *140*, 371–387.

1148　(184) Skempton, A. W. The consolidation of clays by gravitational compaction. *Q. J. Geol. Soc.*
1149　　　　**1970**, *125*, 373–411.

1150　(185) Dewhurst, D. N.; Aplin, A. C.; Sarda, J.-P. Influence of clay fraction on pore-scale
1151　　　　properties and hydraulic conductivity of experimentally compacted mudstones. *J.*
1152　　　　*Geophys. Res.* **1999**, *104*, 29261–29274.

1153　(186) Rutqvist, J.; Tsang, C.-F. A study of caprock hydromechanical changes associated with
1154　　　　CO_2 -injection into a brine formation. *Environ. Geol.* **2002**, *42*, 296–305.

1155　(187) Li, C.; Tien, N.-C.; Zhang, K.; Jen, C.-P.; Hsieh, P.-S.; Huang, S.-Y.; Maggi, F.
1156　　　　Assessment of large-scale offshore CO_2 geological storage in Western Taiwan Basin. *Int.*
1157　　　　*J. Greenh. Gas Control* **2013**, *19*, 281–298.

1158　(188) Rinaldi, A. P.; Rutqvist, J.; Cappa, F. Geomechanical effects on CO_2 leakage through fault
1159　　　　zones during large-scale underground injection. *Int. J. Greenh. Gas Control* **2014**, *20*,
1160　　　　117–131.

1161   (189) Dzevanshir, R. D.; Buryakovskiy, L. A.; Chilingarian, G. V. Simple quantitative
1162   evaluation of porosity of argillaceous sediments at various depths of burial. *Sediment.*
1163   *Geol.* **1986**, *46*, 169–175.

1164   (190) Maubeuge, F.; Lerche, I. Geopressure evolution and hydrocarbon generation in a north
1165   Indonesian basin: two-dimensional quantitative modelling. *Mar. Pet. Geol.* **1994**, *11*, 104–
1166   115.

1167   (191) Luo, X.; Vasseur, G. Geopressuring mechanism of organic matter cracking: numerical
1168   modeling. *Am. Assoc. Pet. Geol. Bull.* **1996**, *80*, 856–874.

1169   (192) Mann, D. M.; Mackenzie, A. S. Prediction of pore fluid pressures in sedimentary basins.
1170   *Mar. Pet. Geol.* **1990**, *7*, 55–65.

1171   (193) Peltonen, C.; Marcussen, Ø.; Bjørlykke, K.; Jahren, J. Clay mineral diagenesis and quartz
1172   cementation in mudstones: The effects of smectite to illite reaction on rock properties.
1173   *Mar. Pet. Geol.* **2009**, *26*, 887–898.

1174   (194) Bowers, G. L.; Katsube, T. J. The role of shale pore structure on the sensitivity of wire-
1175   line logs to overpressure. In *Pressure regimes in sedimentary basins and their prediction:*
1176   *AAPG Memoir 76*; Huffman, A. R., Bowers, G. L., Eds.; American Association of
1177   Petroleum Geologists, 2002; pp 43–60.

1178   (195) Olsen, H. W. Hydraulic flow through saturated clays. *Clays Clay Miner.* **1962**, *9*, 131–
1179   162.

1180   (196) Mills, R. Self-diffusion in normal and heavy water in the range 1-45°. *J. Phys. Chem.*
1181   **1973**, *77*, 685–688.

1182   (197) Bourg, I. C.; Sposito, G.; Bourg, A. C. M. Tracer diffusion in compacted, water-saturated
1183   bentonite. *Clays Clay Miner.* **2006**, *54*, 363–374.

1184   (198) Kohli, A. H.; Zoback, M. D. Frictional properties of shale reservoir rocks. *J. Geophys.*
1185   *Res.: Solid Earth* **2013**, *118*, 5109–5125.

1186   (199) Dutta, P.; Zoback, M. D. CO_2 sequestration into the Wyodak coal seam of Powder River
1187   Basin—Preliminary reservoir characterization and simulation. *Int. J. Greenh. Gas Control*
1188   **2012**, *9*, 103–116.

1189   (200) Wainwright, H. M.; Finsterle, S.; Zhou, Q.; Birkholzer, J. T. Modeling the performance of
1190   large-scale CO_2 storage systems: A comparison of different sensitivity analysis methods.
1191   *Int. J. Greenh. Gas Control* **2013**, *17*, 189–205.

1192   (201) Shukla, R.; Ranjith, P. G.; Choi, S. K.; Haque, A. Study of caprock integrity in
1193   geosequestration of carbon dioxide. *Int. J. Geomech.* **2011**, *11*, 294–301.

1194   (202) Gherardi, F.; Xu, T.; Pruess, K. Numerical modeling of self-limiting and self-enhancing
1195   caprock alteration induced by CO_2 storage in a depleted gas reservoir. *Chem. Geol.* **2007**,
1196   *244*, 103–129.

1197   (203) Deng, H.; Ellis, B. R.; Peters, C. A.; Fitts, J. P.; Crandall, D.; Bromhal, G. S.
1198   Modifications of carbonate fracture hydrodynamic properties by CO_2-acidified brine flow.
1199   *Energy & Fuels* **2013**, *27*, 4221–4231.

1200   (204) Noiriel, C.; Madé, B.; Gouze, P. Impact of coating development on the hydraulic and
1201   transport properties in argillaceous limestone fracture. *Water Resour. Res.* **2007**, *43*,
1202   W09406.

1203   (205) Ellis, B. R.; Fitts, J. P.; Bromhal, G. S.; McIntyre, D. L.; Tappero, R.; Peters, C. A.
1204   Dissolution-driven permeability reduction of a fractured carbonate caprock. *Environ. Eng.*
1205   *Sci.* **2013**, *30*, 187–193.

1206   (206) Kutchko, B. G.; Strazisar, B. R.; Dzombak, D. A.; Lowry, G. V; Thaulow, N. Degradation
1207   of well cement by CO_2 under geologic sequestration conditions. *Environ. Sci. Technol.*
1208   **2007**, *41*, 4787–4792.

1209   (207) Wigand, M.; Kaszuba, J. P.; Carey, J. W.; Hollis, W. K. Geochemical effects of CO_2
1210   sequestration on fractured wellbore cement at the cement/caprock interface. *Chem. Geol.*
1211   **2009**, *265*, 122–133.

1212   (208) Shen, J.; Dangla, P.; Thiery, M. Reactive transport modeling of CO_2 through cementitious
1213   materials under CO_2 geological storage conditions. *Int. J. Greenh. Gas Control* **2013**, *18*,
1214   75–87.

1215   (209) Wolterbeek, T. K. T.; Peach, C. J.; Spiers, C. J. Reaction and transport in wellbore
1216   interfaces under CO_2 storage conditions: Experiments simulating debonded cement-casing
1217   interfaces. *Int. J. Greenh. Gas Control* **2013**, *19*, 519–529.

1218   (210) Matteo, E. N.; Scherer, G. W. Experimental study of the diffusion-controlled acid
1219   degradation of Class H Portland cement. *Int. J. Greenh. Gas Control* **2012**, *7*, 181–191.

1220   (211) Mason, H. E.; Walsh, S. D. C.; DuFrane, W. L.; Carroll, S. A. Determination of diffusion
1221   profiles in altered wellbore cement using X-ray computed tomography methods. *Environ.*
1222   *Sci. Technol.* **2014**, *48*, 7094–7100.

1223   (212) Huerta, N. J.; Hesse, M. A.; Bryant, S. L.; Strazisar, B. R.; Lopano, C. L. Experimental
1224   evidence for self-limiting reactive flow through a fractured cement core: Implications for
1225   time-dependent wellbore leakage. *Environ. Sci. Technol.* **2013**, *47*, 269–275.

1226   (213) Walsh, S. D. C.; Mason, H. E.; Du Frane, W. L.; Carroll, S. A. Mechanical and hydraulic
1227   coupling in cement-caprock interfaces exposed to carbonated brine. *Int. J. Greenh. Gas*
1228   *Control* **2014**, *25*, 109–120.

1229 (214) Jain, A. K.; Juanes, R. Preferential mode of gas invasion in sediments: grain-scale
1230   mechanistic model of coupled multiphase fluid flow and sediment mechanics. *J. Geophys.*
1231   *Res.* **2009**, *114*, B08101.

1232 (215) Alkan, H.; Müller, W. Approaches for modelling gas flow in clay formations as repository
1233   systems. *Phys. Chem. Earth* **2008**, *33*, S260–S268.

1234 (216) Olivella, S.; Alonso, E. E. Gas flow through clay barriers. *Géotechnique* **2008**, *58*, 157–
1235   176.

1236 (217) Carey, J. W.; Svec, R.; Grigg, R.; Zhang, J.; Crow, W. Experimental investigation of
1237   wellbore integrity and CO_2–brine flow along the casing–cement microannulus. *Int. J.*
1238   *Greenh. Gas Control* **2010**, *4*, 272–282.

1239 (218) Duguid, A.; Scherer, G. W. Degradation of oilwell cement due to exposure to carbonated
1240   brine. *Int. J. Greenh. Gas Control* **2010**, *4*, 546–560.

1241 (219) Abdoulghafour, H.; Luquot, L.; Gouze, P. Characterization of the mechanisms controlling
1242   the permeability changes of fractured cements flowed through by CO_2-rich brine. *Environ.*
1243   *Sci. Technol.* **2013**, *47*, 10332–10338.

1244 (220) Wertz, F.; Gherardi, F.; Blanc, P.; Bader, A.-G.; Fabbri, A. Cement CO_2-alteration
1245   propagation at the well–caprock–reservoir interface and influence of diffusion. *Int. J.*
1246   *Greenh. Gas Control* **2013**, *12*, 9–17.

1247 (221) Newell, D. L.; Carey, J. W. Experimental evaluation of wellbore integrity along the
1248   cement-rock boundary. *Environ. Sci. Technol.* **2013**, *47*, 276–282.

1249 (222) Liteanu, E.; Spiers, C. J. Fracture healing and transport properties of wellbore cement in
1250   the presence of supercritical CO_2. *Chem. Geol.* **2011**, *281*, 195–210.

1251 (223) Bourg, I. C.; Tournassat, C. Self-diffusion of water and ions in clay barriers. In *Natural*
1252   *and Engineered Clay Barriers*; Tournassat, C., Steefel, C. I., Bourg, I. C., Bergaya, F.,
1253   Eds.; Developments in Clay Science, Vol. 6; Elsevier, 2015, pp 189-226.

1254 (224) Huet, B. M.; Prevost, J. H.; Scherer, G. W. Quantitative reactive transport modeling of
1255   Portland cement in CO2-saturated water. *Int. J. Greenh. Gas Control* **2010**, *4*, 561–574.

1256 (225) Fernandez-Martinez, A.; Hu, Y.; Lee, B.; Jun, Y.-S.; Waychunas, G. A. In situ
1257   determination of interfacial energies between heterogeneously nucleated $CaCO_3$ and
1258   quartz substrates: Thermodynamics of CO_2 mineral trapping. *Environ. Sci. Technol.* **2013**,
1259   *47*, 102–109.

1260 (226) Li, Q.; Fernandez-Martinez, A.; Lee, B.; Waychunas, G. A.; Jun, Y.-S. Interfacial energies
1261   for heterogeneous nucleation of calcium carbonate on mica and quartz. *Environ. Sci.*
1262   *Technol.* **2014**, *48*, 5745–5753.

1263   (227) Hedges, L. O.; Whitelam, S. Selective nucleation in porous media. *Soft Matter* **2013**, *9*,
1264   9763-9766.

1265   (228) Felmy, A. R.; Qafoku, O.; Arey, B. W.; Hu, J. Z.; Hu, M.; Schaef, H. T.; Ilton, E. S.;
1266   Hess, N. J.; Pearce, C. I.; Feng, J.; et al. Reaction of water-saturated supercritical CO_2
1267   with forsterite: Evidence for magnesite formation at low temperatures. *Geochim.*
1268   *Cosmochim. Acta* **2012**, *91*, 271–282.

1269   (229) Emmanuel, S.; Ague, J. J. Modeling the impact of nano-pores on mineralization in
1270   sedimentary rocks. *Water Resour. Res.* **2009**, *45*, W04406.

1271   (230) Stack, A. G.; Fernandez-Martinez, A.; Allard, L. F.; Bañuelos, J. L.; Rother, G.; Anovitz,
1272   L. M.; Cole, D. R.; Waychunas, G. A. Pore-size-dependent calcium carbonate
1273   precipitation controlled by surface chemistry. *Environ. Sci. Technol.* **2014**, *48*, 6177–
1274   6183.

1275   (231) Anovitz, L. M.; Cole, D. R.; Rother, G.; Allard, L. F.; Jackson, A. J.; Littrell, K. C.
1276   Diagenetic changes in macro- to nano-scale porosity in the St. Peter Sandstone: An (ultra)
1277   small angle neutron scattering and backscattered electron imaging analysis. *Geochim.*
1278   *Cosmochim. Acta* **2013**, *102*, 280–305.

1279   (232) Stack, A. G. Next generation models of carbonate mineral growth and dissolution.
1280   *Greenhouse Gas Sci. Technol.* **2014**, *11*, 1–11.

1281   (233) Putnis, A.; Mauthe, G. The effect of pore size on cementation in porous rocks. *Geofluids*
1282   **2001**, *1*, 37–41.

1283   (234) Gonçalvès, J.; Rousseau-Gueutin, P.; Revil, A. Introducing interacting diffuse layers in
1284   TLM calculations: a reappraisal of the influence of the pore size on the swelling pressure
1285   and the osmotic efficiency of compacted bentonites. *J. Colloid Interface Sci.* **2007**, *316*,
1286   92–99.

1287   (235) Espinoza, D. N.; Santamarina, J. C. Clay interaction with liquid and supercritical CO_2:
1288   The relevance of electrical and capillary forces. *Int. J. Greenh. Gas Control* **2012**, *10*,
1289   351–362.

1290   (236) Michot, L. J.; Bihannic, I.; Thomas, F.; Lartiges, B. S.; Waldvogel, Y.; Caillet, C.;
1291   Thieme, J.; Funari, S. S.; Levitz, P. Coagulation of Na-montmorillonite by inorganic
1292   cations at neutral pH. A combined transmission X-ray microscopy, small angle and wide
1293   angle X-ray scattering study. *Langmuir* **2013**, *29*, 3500–3510.

1294   (237) Sarout, J.; Detournay, E. Chemoporoelastic analysis and experimental validation of the
1295   pore pressure transmission test for reactive shales. *Int. J. Rock Mech. Min. Sci.* **2011**, *48*,
1296   759–772.

1297 (238) Ilton, E. S.; Schaef, H. T.; Qafoku, O.; Rosso, K. M.; Felmy, A. R. In situ X-ray
1298   diffraction study of Na^+ saturated montmorillonite exposed to variably wet super critical
1299   CO2. *Environ. Sci. Technol.* **2012**, *46*, 4241–4248.

1300 (239) de Jong, S. M.; Spiers, C. J.; Busch, A. Development of swelling strain in smectite clays
1301   through exposure to carbon dioxide. *Int. J. Greenh. Gas Control* **2014**, *24*, 149–161.

1302 (240) Loring, J. S.; Schaef, H. T.; Turcu, R. V. F.; Thompson, C. J.; Miller, Q. R. S.; Martin, P.
1303   F.; Hu, J.; Hoyt, D. W.; Qafoku, O.; Ilton, E. S.; et al. In situ molecular spectroscopic
1304   evidence for CO_2 intercalation into montmorillonite in supercritical carbon dioxide.
1305   *Langmuir* **2012**, *28*, 7125–7128.

1306 (241) Botan, A.; Rotenberg, B.; Marry, V.; Turq, P.; Noetinger, B. Carbon dioxide in
1307   montmorillonite clay hydrates: Thermodynamics, structure, and transport from molecular
1308   simulation. *J. Phys. Chem. C* **2010**, *114*, 14962–14969.

1309 (242) Rother, G.; Ilton, E. S.; Wallacher, D.; Hauss, T.; Schaef, H. T.; Qafoku, O.; Rosso, K.
1310   M.; Felmy, A. R.; Krukowski, E. G.; Stack, A. G.; et al. CO_2 sorption to subsingle
1311   hydration layer montmorillonite clay studied by excess sorption and neutron diffraction
1312   measurements. *Environ. Sci. Technol.* **2013**, *47*, 205–211.

1313 (243) Giesting, P.; Guggenheim, S.; Koster van Groos, A. F.; Busch, A. X-ray diffraction study
1314   of K- and Ca-exchanged montmorillonites in CO_2 atmospheres. *Environ. Sci. Technol.*
1315   **2012**, *46*, 5623–5630.

1316 (244) Suekane, T.; Nobuso, T.; Hirai, S.; Kiyota, M. Geological storage of carbon dioxide by
1317   residual gas and solubility trapping. *Int. J. Greenh. Gas Control* **2008**, *2*, 58–64.

1318 (245) Chiquet, P.; Broseta, D.; Thibeau, S. Wettability alteration of caprock minerals by carbon
1319   dioxide. *Geofluids* **2007**, *7*, 112–122.

1320 (246) LaForce, T.; Ennis-King, J.; Boreham, C.; Paterson, L. Residual CO_2 saturation estimate
1321   using noble gas tracers in single-well field test: The CO2CRC Otway project. *Int. J.*
1322   *Greenh. Gas Control* **2014**, *26*, 9–21.

1323 (247) Plug, W.-J.; Bruining, J. Capillary pressure for the sand–CO_2–water system under various
1324   pressure conditions. Application to CO_2 sequestration. *Adv. Water Resour.* **2007**, *30*,
1325   2339–2353.

1326 (248) Bachu, S.; Bennion, B. Effects of in-situ conditions on relative permeability
1327   characteristics of CO_2-brine systems. *Environ. Geol.* **2008**, *54*, 1707–1722.

1328 (249) Iglauer, S.; Paluszny, A.; Pentland, C. H.; Blunt, M. J. Residual CO_2 imaged with X-ray
1329   micro-tomography. *Geophys. Res. Lett.* **2011**, *38*, L21403.

1330 (250) Pentland, C. H.; El-Maghraby, R.; Iglauer, S.; Blunt, M. J. Measurements of the capillary
1331   trapping of super   critical carbon dioxide in Berea sandstone. *Geophys. Res. Lett.* **2011**,
1332   *38*, L06401.

1333 (251) Shi, J.-Q.; Xue, Z.; Durucan, S. Supercritical CO_2 core flooding and imbibition in Tako
1334   sandstone—Influence of sub-core scale heterogeneity. *Int. J. Greenh. Gas Control* **2011**,
1335   *5*, 75–87.

1336 (252) Krevor, S. C. M.; Pini, R.; Zuo, L.; Benson, S. M. Relative permeability and trapping of
1337 CO_2 and water in sandstone rocks at reservoir conditions. *Water Resour. Res.* **2012**, *48*,
1338   W02532.

1339 (253) Tanino, Y.; Blunt, M. J. Capillary trapping in sandstones and carbonates: Dependence on
1340   pore structure. *Water Resour. Res.* **2012**, *48*, W08525.

1341 (254) Chaudhary, K.; Cardenas, M. B..; Wolfe, W. W.; Maisano, J. A.; Ketcham, R. A.; Bennett,
1342   P. C. Pore-scale trapping of supercritical CO_2 and the role of grain wettability and shape.
1343   *Geophys. Res. Lett.* **2013**, *40*, 3878–3882.

1344 (255) Andrew, M.; Bijeljic, B.; Blunt, M. J. Pore-scale imaging of trapped supercritical carbon
1345   dioxide in sandstones and carbonates. *Int. J. Greenh. Gas Control* **2014**, *22*, 1–14.

1346 (256) Ruprecht, C.; Pini, R.; Falta, R.; Benson, S.; Murdoch, L. Hysteretic trapping and relative
1347   permeability of CO_2 in sandstone at reservoir conditions. *Int. J. Greenh. Gas Control*
1348   **2014**, *27*, 15–27.

1349 (257) El-Maghraby, R. M.; Blunt, M. J. Residual CO_2 trapping in Indiana limestone. *Environ.*
1350   *Sci. Technol.* **2013**, *47*, 227–233.

1351 (258) Müller, N. Supercritical CO_2-brine relative permeability experiments in reservoir rocks—
1352   Literature review and recommendations. *Transp. Porous Media* **2011**, *87*, 367–383.

1353 (259) Land, C. S. Calculation of imbibition relative permeability for two- and three-phase flow
1354   from rock properties. In *SPE 42nd Annual Fall Meeting, Houston, Texas, 1-4 October*
1355   *1967*; SPE Paper 1942, Society of Petroleum Engineers, 1968.

1356 (260) Li, Y.; Wardlaw, N. C. The influence of wettability and critical pore-throat size ratio on
1357   snap-off. *J. Colloid Interface Sci.* **1986**, *109*, 461–472.

1358 (261) Lenormand, R.; Touboul, E.; Zarcone, C. Numerical models and experiments on
1359   immiscible displacements in porous media. *J. Fluid Mech.* **1988**, *189*, 165–187.

1360 (262) Jerauld, G. R.; Salter, S. J. The effect of pore-structure on hysteresis in relative
1361   permeability and capillary pressure: Pore-level modeling. *Transp. Porous Media* **1990**, *5*,
1362   103–151.

1363   (263) Morrow, N. Wettability and its effect on oil recovery. *SPE J.* **1990**, *42*, 1476–1484.

1364   (264) Blunt, M. J.; Scher, H. Pore-level modeling of wetting. *Phys. Rev. E* **1995**, *52*, 6387–6403.

1365   (265) Jadhunandan, P. P.; Morrow, N. R. Effect of wettability on waterflood recovery for crude-
1366   oil/brine/rock systems. *SPE Reserv. Eng.* **1995**, *10*, 40–46.

1367   (266) Al-Futaisi, A.; Patzek, T. W. Impact of wettability alteration on two-phase flow
1368   characteristics of sandstones: A quasi-static description. *Water Resour. Res.* **2003**, *39*,
1369   1042.

1370   (267) Spiteri, E. J.; Juanes, R.; Blunt, M. J.; Orr, F. M., Jr. A new model of trapping and relative
1371   permeability hysteresis for all wettability characteristics. In *2005 SPE Annual Technical
1372   Conference and Exhibition, Dallas, Texas, 9-12 October*; 2005; SPE Paper 96448, Society
1373   of Petroleum Engineers, 2008.

1374   (268) Pini, R.; Benson, S. M. Simultaneous determination of capillary pressure and relative
1375   permeability curves from core-flooding experiments with various fluid pairs. *Water
1376   Resour. Res.* **2013**, *49*, 3516–3530.

1377   (269) Zuo, L.; Benson, S. M. Process-dependent residual trapping of CO_2 in sandstone.
1378   *Geophys. Res. Lett.* **2014**, *41*, 2820–2826.

1379   (270) Krevor, S. C. M.; Pini, R.; Li, B.; Benson, S. M. Capillary heterogeneity trapping of CO_2
1380   in a sandstone rock at reservoir conditions. *Geophys. Res. Lett.* **2011**, *38*, L15401.

1381   (271) Herring, A. L.; Harper, E. J.; Andersson, L.; Sheppard, A.; Bay, B. K.; Wildenschild, D.
1382   Effect of fluid topology on residual nonwetting phase trapping: Implications for geologic
1383 CO_2 sequestration. *Adv. Water Resour.* **2013**, *62*, 47–58.

1384   (272) Tokunaga, T. K.; Wan, J.; Jung, J.-W.; Kim, T. W.; Kim, Y.; Dong, W. Capillary pressure
1385   and saturation relations for supercritical CO_2 and brine in sand: High-pressure $P_c(S_w)$
1386   controller/meter measurements and capillary scaling predictions. *Water Resour. Res.*
1387   **2013**, *49*, 1–14.

1388   (273) Akbarabadi, M.; Piri, M. Relative permeability hysteresis and capillary trapping
1389   characteristics of supercritical CO_2/brine systems: An experimental study at reservoir
1390   conditions. *Adv. Water Resour.* **2013**, *52*, 190–206.

1391   (274) Ide, S. T.; Jessen, K.; Orr, F. M., Jr. Storage of CO_2 in saline aquifers: Effects of gravity,
1392   viscous, and capillary forces on amount and timing of trapping. *Int. J. Greenh. Gas
1393   Control* **2007**, *1*, 481–491.

1394   (275) Qi, R.; LaForce, T. C.; Blunt, M. J. Design of carbon dioxide storage in aquifers. *Int. J.
1395   Greenh. Gas Control* **2009**, *3*, 195–205.

1396   (276) Alkan, H.; Cinar, Y.; Ülker, E. B. Impact of Capillary Pressure, Salinity and In situ
1397   Conditions on CO2 Injection into Saline Aquifers. *Transp. Porous Media* **2010**, *84*, 799–
1398   819.

1399   (277) Ellis, J. S.; Bazylak, A. Dynamic pore network model of surface heterogeneity in brine-
1400   filled porous media for carbon sequestration. *Phys. Chem. Chem. Phys.* **2012**, *14*, 8382–
1401   8390.

1402   (278) Silin, D.; Tomutsa, L.; Benson, S. M.; Patzek, T. W. Microtomography and pore-scale
1403   modeling of two-phase fluid distribution. *Transp. Porous Media* **2011**, *86*, 495–515.

1404   (279) Li, S.; Dong, M.; Li, Z.; Huang, S.; Qing, H.; Nickel, E. Gas breakthrough pressure for
1405   hydrocarbon reservoir seal rocks: implications for the security of long-term CO_2 storage in
1406   the Weyburn field. *Geofluids* **2005**, *5*, 326–334.

1407   (280) Herring, A. L.; Andersson, L.; Newell, D. L.; Carey, J. W.; Wildenschild, D. Pore-scale
1408   observations of supercritical CO_2 drainage in Bentheimer sandstone by synchrotron x-ray
1409   imaging. *Int. J. Greenh. Gas Control* **2014**, *25*, 93–101.

1410   (281) Wang, S.; Tokunaga, T. K. Capillary pressure - saturation relations for supercritical CO_2
1411   and brine in limestone/dolomite sands: Implications for geologic carbon sequestration in
1412   carbonate reservoirs. *Environ. Sci. Technol.* **2015**, *49*, 7208–7217.

1413   (282) Kim, Y.; Wan, J.; Kneafsey, T. J.; Tokunaga, T. K. Dewetting of silica surfaces upon
1414   reactions with supercritical CO_2 and brine: pore-scale studies in micromodels. *Environ.*
1415   *Sci. Technol.* **2012**, *46*, 4228–4235.

1416   (283) Kovscek, A. R.; Wong, H.; Radke, C. J. A pore-level scenario for the development of
1417   mixed wettability in oil reservoirs. *AIChE J.* **1993**, *39*, 1072–1085.

1418   (284) Dickson, J. L.; Gupta, G.; Horozov, T. S.; Binks, B. P.; Johnston, K. P. Wetting
1419   phenomena at the CO_2/water/glass interface. *Langmuir* **2006**, *22*, 2161–2170.

1420   (285) Siemons, N.; Bruining, H.; Castelijns, H.; Wolf, K.-H. Pressure dependence of the contact
1421   angle in a CO_2-H_2O-coal system. *J. Colloid Interface Sci.* **2006**, *297*, 755–761.

1422   (286) Yang, D.; Gu, Y.; Tontiwachwuthikul, P. Wettability determination of the reservoir brine-
1423   reservoir rock system with dissolution of CO_2 at high pressures and elevated temperatures.
1424   *Energy & Fuels* **2008**, *22*, 504–509.

1425   (287) Chalbaud, C.; Robin, M.; Lombard, J.-M.; Martin, F.; Egermann, P.; Bertin, H. Interfacial
1426   tension measurements and wettability evaluation for geological CO_2 storage. *Adv. Water*
1427   *Resour.* **2009**, *32*, 98–109.

1428   (288) Espinoza, D. N.; Santamarina, J. C. Water-CO_2-mineral systems: Interfacial tension,
1429   contact angle, and diffusion—Implications to CO_2 geological storage. *Water Resour. Res.*
1430   **2010**, *46*, W07537.

1431   (289) Tonnet, N.; Shah, V.; Chiquet, P.; Diaz, J.; Mouronval, G.; Broseta, D. Wettability
1432   alteration of caprock minerals by acid gases. In *The 10th Wettability conference, Abu*
1433   *Dhabi, UAE, Oct. 27-28.*; 2008.

1434   (290) Shah, V.; Broseta, D.; Mouronval, G. Capillary alteration of caprocks by acid gases. In
1435   *SPE/DOE Symposium on Improved Oil Recovery, Tulsa, OK*; SPE Paper 113353, Society
1436   of Petroleum Engineers, 2008.

1437   (291) Bikkina, P. K. Contact angle measurements of CO_2-water-quartz/calcite systems in the
1438   perspective of carbon sequestration. *Int. J. Greenh. Gas Control* **2011**, *5*, 1259–1271.

1439   (292) Mills, J.; Riazi, M.; Sohrabi, M. Wettability of common rock-forming minerals in a CO_2-
1440   brine system at reservoir conditions. In *Proceedings of the International Symposium of the*
1441   *Society of Core Analysts, Austin, TX*; SCA2011-06, Society of Core Analysts, 2011.

1442   (293) Jung, J.; Wan, J. Supercritical CO_2 and ionic strength effects on wettability of silica
1443   surfaces: Equilibrium contact angle measurements. *Energy & Fuels* **2012**, *26*, 6053–6059.

1444   (294) Broseta, D.; Tonnet, N.; Shah, V. Are rocks still water-wet in the presence of dense CO_2
1445   or H_2S? *Geofluids* **2012**, *12*, 280–294.

1446   (295) Farokhpoor, R.; Bjørkvik, B. J. A.; Lindeberg, E.; Torsæter, O. Wettability behaviour of
1447 CO_2 at storage conditions. *Int. J. Greenh. Gas Control* **2013**, *12*, 18–25.

1448   (296) Saraji, S.; Goual, L.; Piri, M.; Plancher, H. Wettability of supercritical carbon
1449   dioxide/water/quartz systems: simultaneous measurement of contact angle and interfacial
1450   tension at reservoir conditions. *Langmuir* **2013**, *29*, 6856–6866.

1451   (297) Wang, S.; Edwards, I. M.; Clarens, A. F. Wettability phenomena at the CO_2-brine-mineral
1452   interface: Implications for geologic carbon sequestration. *Environ. Sci. Technol.* **2013**, *47*,
1453   234–241.

1454   (298) Wang, S.; Tao, Z.; Persily, S. M.; Clarens, A. F. CO_2 adhesion on hydrated mineral
1455   surfaces. *Environ. Sci. Technol.* **2013**, *47*, 11858–11865.

1456   (299) Wesch, A.; Dahmen, N.; Ebert, K.; Schön, J. Grenzflächenspannungen, tropfengrössen
1457   und kontaktwinkel in zweiphasensystem H_2O/CO_2 bein temperaturen von 298 bis 333 K
1458   under drücken bis 30 MPa. *Chemie Ing. Tech.* **1997**, *69*, 942–946.

1459   (300) Wan, J.; Kim, Y.; Tokunaga, T. K. Contact angle measurement ambiguity in supercritical
1460 CO_2–water–mineral systems: Mica as an example. *Int. J. Greenh. Gas Control* **2014**, *31*,
1461   128–137.

1462   (301) Liu, S.; Yang, X.; Qin, Y. Molecular dynamics simulation of wetting behavior at
1463 CO_2/water/solid interfaces. *Chinese Sci. Bull.* **2010**, *55*, 2252–2257.

1464   (302) Bagherzadeh, S. A.; Englezos, P.; Alavi, S.; Ripmeester, J. A. Influence of hydrated silica
1465   surfaces on interfacial water in the presence of clathrate hydrate forming gases. *J. Phys.*
1466   *Chem. C* **2012** *116*, 24907-24915.

1467   (303) Iglauer, S.; Mathew, M. S.; Bresme, F. Molecular dynamics computations of brine-CO_2
1468   interfacial tensions and brine-CO_2-quartz contact angles and their effects on structural and
1469   residual trapping mechanisms in carbon geo-sequestration. *J. Colloid Interface Sci.* **2012**,
1470   *386*, 405–414.

1471   (304) Tenney, C. M.; Cygan, R. T. Molecular simulation of carbon dioxide, brine, and clay
1472   mineral interactions and determination of contact angles. *Environ. Sci. Technol.* **2014**, *48*,
1473   2035–2042.

1474   (305) McCaughan, J.; Iglauer, S.; Bresme, F. Molecular dynamics simulation of water/CO_2-
1475   quartz interfacial properties: Application to subsurface gas injection. *Energy Procedia*
1476   **2013**, *37*, 5387–5402.

1477   (306) Hamm, L. M.; Bourg, I. C.; Wallace, A. F.; Rotenberg, B. Molecular simulation of CO_2-
1478   and CO_3-brine-mineral systems. *Rev. Mineral. Geochemistry* **2013**, *77*, 189–228.

1479   (307) Iglauer, S.; Salamah, A.; Sarmadivaleh, M.; Liu, K.; Phan, C. Contamination of silica
1480   surfaces: Impact on water-CO_2-quartz and glass contact angle measurements. *Int. J.*
1481   *Greenh. Gas Control* **2014**, *22*, 325–328.

1482   (308) Lamb, R. N.; Furlong, D. N. Controlled wettability of quartz surfaces. *J. Chem. Soc.*
1483   *Faraday Trans. 1* **1982**, *78*, 61-73.

1484   (309) Chiquet, P.; Daridon, J.-L.; Broseta, D.; Thibeau, S. CO_2/water interfacial tensions under
1485   pressure and temperature conditions of CO_2 geological storage. *Energy Convers. Manag.*
1486   **2007**, *48*, 736–744.

1487   (310) Kvamme, B.; Kuznetsova, T.; Hebach, A.; Oberhof, A.; Lunde, E. Measurements and
1488   modelling of interfacial tension for water+carbon dioxide systems at elevated pressures.
1489   *Comput. Mater. Sci.* **2007**, *38*, 506–513.

1490   (311) Aggelopoulos, C. A.; Robin, M.; Vizika, O. Interfacial tension between CO_2 and brine
1491   ($NaCl$+$CaCl_2$) at elevated pressures and temperatures: The additive effect of different
1492   salts. *Adv. Water Resour.* **2011**, *34*, 505–511.

1493   (312) Georgiadis, A.; Maitland, G.; Trusler, J. P. M.; Bismarck, A. Interfacial tension
1494   measurements of the (H_2O + CO_2) system at elevated pressures and temperatures. *J.*
1495   *Chem. Eng. Data* **2010**, *55*, 4168–4175.

1496   (313) Hebach, A.; Oberhof, A.; Dahmen, N.; Kögel, A.; Ederer, H.; Dinjus, E. Interfacial
1497   tension at elevated pressures - Measurements and correlations in the water + carbon
1498   dioxide system. *J. Chem. Eng. Data* **2002**, *47*, 1540–1546.

1499   (314) Li, X.; Boek, E. S.; Maitland, G. C.; Trusler, J. P. M. Interfacial tension of (brines + CO_2):
1500 $CaCl_2$(aq), $MgCl_2$(aq), and Na_2SO_4(aq) at temperatures between (343 and 423) K,
1501   pressures between (2 and 50) MPa, and total molalities of (0.5 to 5) mol kg^{-1}. *J. Chem.*
1502   *Eng. Data* **2012**, *57*, 1369–1375.

1503   (315) Nielsen, L. C.; Bourg, I. C.; Sposito, G. Predicting CO_2–water interfacial tension under
1504   pressure and temperature conditions of geologic CO_2 storage. *Geochim. Cosmochim. Acta*
1505   **2012**, *81*, 28–38.

1506   (316) Liu, Y.; Lafitte, T.; Panagiotopoulos, A. Z.; Debenedetti, P. G. Simulations of vapor-
1507   liquid phase equilibrium and interfacial tension in the CO_2-H_2O-NaCl system. *AIChE J.*
1508   **2013**, *59*, 3514–3522.

1509   (317) Li, X.; Ross, D. A.; Trusler, J. P. M.; Maitland, G. C.; Boek, E. S. Molecular dynamics
1510   simulations of CO_2 and brine interfacial tension at high temperatures and pressures. *J.*
1511   *Phys. Chem. B* **2013**, *117*, 5647–5652.

1512   (318) Banerjee, S.; Hassenklöver, E.; Kleijn, J. M.; Cohen Stuart, M. A.; Leermakers, F. A. M.
1513   Interfacial tension and wettability in water-carbon dioxide systems: experiments and self-
1514   consistent field modeling. *J. Phys. Chem. B* **2013**, *117*, 8524–8235.

1515   (319) Duchateau, C.; Broseta, D. A simple method for determining brine–gas interfacial
1516   tensions. *Adv. Water Resour.* **2012**, *42*, 30–36.

1517   (320) Butt, H.; Graf, K.; Kappl, M. *Physics and Chemistry of Interfaces, 2nd ed.*; Wiley-VCH:
1518   Weinheim, 2006.

1519   (321) Loring, J. S.; Thompson, C. J.; Wang, Z.; Joly, A. G.; Sklarew, D. S.; Schaef, H. T.; Ilton,
1520   E. S.; Rosso, K. M.; Felmy, A. R. In situ infrared spectroscopic study of forsterite
1521   carbonation in wet supercritical CO_2. *Environ. Sci. Technol.* **2011**, *45*, 6204–6210.

1522   (322) Kerisit, S.; Weare, J. H.; Felmy, A. R. Structure and dynamics of forsterite–$scCO_2$/H_2O
1523   interfaces as a function of water content. *Geochim. Cosmochim. Acta* **2012**, *84*, 137–151.

1524   (323) Kim, T. W.; Tokunaga, T. K.; Shuman, D. B.; Sutton, S. R.; Newville, M.; Lanzirotti, A.
1525   Thickness measurements of nanoscale brine films on silica surfaces under geologic CO_2
1526   sequestration conditions using synchrotron X-ray fluorescence. *Water Resour. Res.* **2012**,
1527   *48*, W09558.

1528   (324) Churaev, N. V. Surface forces in wetting films. *Adv. Colloid Interface Sci.* **2003**, *103*,
1529   197–218.

1530 (325) Tripp, C. P.; Combes, J. R. Chemical modification of metal oxide surfaces in supercritical
1531 CO_2: The interaction of supercritical CO_2 with the adsorbed water layer and the surface
1532   hydroxyl groups of a silica surface. *Langmuir* **1998**, *14*, 7348–7352.

1533 (326) Cole, D. R.; Chialvo, A. A.; Rother, G.; Vlcek, L.; Cummings, P. T. Supercritical fluid
1534   behavior at nanoscale interfaces: Implications for CO_2 sequestration in geologic
1535   formations. *Philos. Mag.* **2010**, *90*, 2339–2363.

1536 (327) Lagneau, V.; Pipart, A.; Catalette, H. Reactive transport modelling of CO_2 sequestration in
1537   deep saline aquifers. *Oil Gas Sci. Technol.* **2005**, *60*, 231–247.

1538 (328) Kaszuba, J.; Yardley, B.; Andreani, M. Experimental perspectives of mineral dissolution
1539   and precipitation due to carbon dioxide-water-rock interactions. *Rev. Mineral.*
1540   *Geochemistry* **2013**, *77*, 153–188.

1541 (329) Zheng, F.; Shi, X. Q.; Wu, J. C.; Chen, Y.; Xu, H. X. Global sensitivity analysis of
1542   reactive transport modeling of CO_2 geological storage in a saline aquifer. *Procedia Earth*
1543   *Planet. Sci.* **2013**, *7*, 798–801.

1544 (330) Worden, R. H. Dawsonite cement in the Triassic Lam Formation, Shabwa Basin, Yemen:
1545   A natural analogue for a potential mineral product of subsurface CO_2 storage for
1546   greenhouse gas reduction. *Mar. Pet. Geol.* **2006**, *23*, 61–77.

1547 (331) Pauwels, H.; Gaus, I.; le Nindre, Y. M.; Pearce, J.; Czernichowski-Lauriol, I. Chemistry of
1548   fluids from a natural analogue for a geological CO_2 storage site (Montmiral, France):
1549   Lessons for CO_2–water–rock interaction assessment and monitoring. *Appl. Geochemistry*
1550   **2007**, *22*, 2817–2833.

1551 (332) Heinemann, N.; Wilkinson, M.; Haszeldine, R. S.; Fallick, A. E.; Pickup, G. E. CO_2
1552   sequestration in a UK North Sea analogue for geological carbon storage. *Geology* **2013**,
1553   *41*, 411–414.

1554 (333) Armstrong, R.; Ajo-Franklin, J. Investigating biomineralization using synchrotron based
1555   X-ray computed microtomography. *Geophys. Res. Lett.* **2011**, *38*, L08406.

1556 (334) Nogues, J. P.; Fitts, J. P.; Celia, M. A.; Peters, C. A. Permeability evolution due to
1557   dissolution and precipitation of carbonates using reactive transport modeling in pore
1558   networks. *Water Resour. Res.* **2013**, *49*, 6006–6021.

1559 (335) Wendler, J.; Köster, J.; Götze, J.; Kasch, N.; Zisser, N.; Kley, J.; Pudlo, D.; Nover, G.;
1560   Gaupp, R. Carbonate diagenesis and feldspar alteration in fracture-related bleaching zones
1561   (Buntsandstein, central Germany): possible link to CO_2-influenced fluid–mineral
1562   reactions. *Int. J. Earth Sci.* **2011**, *101*, 159–176.

1563 (336) Liu, F.; Lu, P.; Griffith, C.; Hedges, S. W.; Soong, Y.; Hellevang, H.; Zhu, C. CO_2-brine-
1564　　　　caprock interaction: Reactivity experiments on Eau Claire shale and a review of relevant
1565　　　　literature. *Int. J. Greenh. Gas Control* **2012**, *7*, 153–167.

1566 (337) Helgeson, H. C.; Murphy, W. M.; Aagaard, P. Thermodynamic and kinetic constraints on
1567　　　　reaction rates among minerals and aqueous solutions. II. Rate constants, effective surface
1568　　　　area, and the hydrolysis of feldspar. *Geochim. Cosmochim. Acta* **1984**, *48*, 2405–2432.

1569 (338) Brosse, É.; Magnier, C.; Vincent, B. Modelling fluid-rock interaction induced by the
1570　　　　percolation of CO_2-enriched solutions in core samples: The role of reactive surface area.
1571　　　　*Oil Gas Sci. Technol.* **2005**, *60*, 287–305.

1572 (339) Maher, K.; Steefel, C. I.; White, A. F.; Stonestrom, D. A. The role of reaction affinity and
1573　　　　secondary minerals in regulating chemical weathering rates at the Santa Cruz Soil
1574　　　　Chronosequence, California. *Geochim. Cosmochim. Acta* **2009**, *73*, 2804–2831.

1575 (340) Alemu, B. L.; Aagaard, P.; Munz, I. A.; Skurtveit, E. Caprock interaction with CO_2: A
1576　　　　laboratory study of reactivity of shale with supercritical CO_2 and brine mixtures at 250°C
1577　　　　and 110 bars. *Appl. Geochemistry* **2011**, *26*, 1975–1989.

1578 (341) Carroll, S. A.; McNab, W. W.; Torres, S. C. Experimental study of cement-
1579　　　　sandstone/shale-brine-CO_2 interactions. *Geochem. Trans.* **2011**, *12*, 9.

1580 (342) White, A. F.; Brantley, S. L. The effect of time on the weathering of silicate minerals: why
1581　　　　do weathering rates differ in the laboratory and field? *Chem. Geol.* **2003**, *202*, 479–506.

1582 (343) Gadikota, G.; Swanson, E. J.; Zhao, H.; Park, A.-H. A. Experimental design and data
1583　　　　analysis for accurate estimation of reaction kinetics and conversion for carbon
1584　　　　mineralization. *Ind. Eng. Chem. Res.* **2014**, *53*, 6664–6676.

1585 (344) Wolery, T. J.; Jackson, K. J.; Bourcier, W. L.; Burton, C.J.; Viani, B. E.; Knauss, K. G.;
1586　　　　Delany, J. M. Current Status of the EQ3/6 Software Package for Geochemical Modeling.
1587　　　　*ACS Symp. Series* **1990**, *416*, 104–116.

1588 (345) Palandri, J. L.; Kharaka, Y. K. *A compilation of rate parameters of water-mineral
1589　　　　interaction kinetics for application to geochemical modeling*; Open File Report 2004-
1590　　　　1068, US Geological Survey, 2004.

1591 (346) Johnson, J. W.; Oelkers, E. H.; Helgeson, H. C. SUPCRT92: A software package for
1592　　　　calculating the standard molal thermodynamic properties of minerals, gases, aqueous
1593　　　　species, and reactions from 1 to 5000 bar and 0 to 1000°C. *Comput. Geosci.* **1992**, *18*,
1594　　　　899–947.

1595 (347) Dethlefsen, F.; Haase, C.; Ebert, M.; Dahmke, A. Uncertainties of geochemical modeling
1596　　　　during CO_2 sequestration applying batch equilibrium calculations. *Environ. Earth Sci.*
1597　　　　**2012**, *65*, 1105–1117.

1598 (348) Haase, C.; Dethlefsen, F.; Ebert, M.; Dahmke, A. Uncertainty in geochemical modelling
1599   of CO_2 and calcite dissolution in NaCl solutions due to different modelling codes and
1600   thermodynamic databases. *Appl. Geochemistry* **2013**, *33*, 306–317.

1601 (349) Fischer, S.; Liebscher, A.; De Lucia, M.; Hecht, L.; the Ketzin Team. Reactivity of
1602   sandstone and siltstone samples from the Ketzin pilot CO_2 storage site-Laboratory
1603   experiments and reactive geochemical modeling. *Environ. Earth Sci.* **2013**, *70*, 3687–
1604   3708.

1605 (350) Shao, H.; Ray, J. R.; Jun, Y.-S. Dissolution and precipitation of clay minerals under
1606   geologic CO_2 sequestration conditions: CO_2-brine-phlogopite interactions. *Environ. Sci.*
1607   *Technol.* **2010**, *44*, 5999–6005.

1608 (351) Shao, H.; Ray, J. R.; Jun, Y.-S. Effects of salinity and the extent of water on supercritical
1609 CO_2-induced phlogopite dissolution and secondary mineral formation. *Environ. Sci.*
1610   *Technol.* **2011**, *45*, 1737–1743.

1611 (352) Bilinski, H.; Horvath, L.; Ingri, N.; Sjöberg, S. Aluminosilicate phases during initial clay
1612   formation: H^+-Al^{3+}-oxalic acid-silicic acid-Na^+ system. *J. Soil Sci.* **1990**, *41*, 119–132.

1613 (353) Koenen, M.; Wasch, L. J.; van Zalinge, M. E.; Nelskamp, S. Werkendam, the Dutch
1614   natural analogue for CO_2 storage – long-term mineral reactions. *Energy Procedia* **2013**,
1615   *37*, 3452–3460.

1616 (354) Yang, Y.; Min, Y.; Jun, Y.-S. Effects of Al/Si ordering on feldspar dissolution: Part II.
1617   The pH dependence of plagioclases' dissolution rates. *Geochim. Cosmochim. Acta* **2014**,
1618   *126*, 595–613.

1619 (355) Yang, L.; Steefel, C. I. Kaolinite dissolution and precipitation kinetics at 22°C and pH 4.
1620   *Geochim. Cosmochim. Acta* **2008**, *72*, 99–116.

1621 (356) Hellevang, H.; Pham, V. T. H.; Aagaard, P. Kinetic modelling of CO_2–water–rock
1622   interactions. *Int. J. Greenh. Gas Control* **2013**, *15*, 3–15.

1623 (357) Saldi, G. D.; Jordan, G.; Schott, J.; Oelkers, E. H. Magnesite growth rates as a function of
1624   temperature and saturation state. *Geochim. Cosmochim. Acta* **2009**, *73*, 5646–5657.

1625 (358) Lu, P.; Fu, Q.; Seyfried, W. E. J.; Hedges, S. W.; Soong, Y.; Jones, K.; Zhu, C. Coupled
1626   alkali feldspar dissolution and secondary mineral precipitation in batch systems – 2: New
1627   experiments with supercritical CO_2 and implications for carbon sequestration. *Appl.*
1628   *Geochemistry* **2013**, *30*, 75–90.

1629 (359) Carroll, S. A.; Knauss, K. G. Dependence of labradorite dissolution kinetics on $CO_{2(aq)}$,
1630 $Al_{(aq)}$, and temperature. *Chem. Geol.* **2005**, *217*, 213–225.

1631 (360) Hänchen, M.; Prigiobbe, V.; Baciocchi, R.; Mazzotti, M. Precipitation in the Mg-
1632 carbonate system—effects of temperature and CO_2 pressure. *Chem. Eng. Sci.* **2008**, *63*,
1633 1012–1028.

1634 (361) Hellmann, R.; Daval, D.; Tisserand, D. The dependence of albite feldspar dissolution
1635 kinetics on fluid saturation state at acid and basic pH: Progress towards a universal
1636 relation. *Comptes Rendus Geosci.* **2010**, *342*, 676–684.

1637 (362) Daval, D.; Hellmann, R.; Martinez, I.; Gangloff, S.; Guyot, F. Lizardite serpentine
1638 dissolution kinetics as a function of pH and temperature, including effects of elevated
1639 pCO_2. *Chem. Geol.* **2013**, *351*, 245–256.

1640 (363) Hu, Y.; Ray, J. R.; Jun, Y.-S. Na^+, Ca^{2+}, and Mg^{2+} in brines affect supercritical CO_2-brine-
1641 biotite interactions: ion exchange, biotite dissolution, and illite precipitation. *Environ. Sci.*
1642 *Technol.* **2013**, *47*, 191–197.

1643 (364) Amin, S. M.; Weiss, D. J.; Blunt, M. J. Reactive transport modelling of geologic CO_2
1644 sequestration in saline aquifers: The influence of pure CO_2 and of mixtures of CO_2 with
1645 CH_4 on the sealing capacity of cap rock at 37 °C and 100 bar. *Chem. Geol.* **2014**, *367*, 39–
1646 50.

1647 (365) Crockford, P.; Telmer, K.; Best, M. Dissolution kinetics of Devonian carbonates at
1648 circum-neutral pH, 50 bar pCO_2, 105 °C, and 0.4 M: The importance of complex brine
1649 chemistry on reaction rates. *Appl. Geochemistry* **2014**, *41*, 128–134.

1650 (366) McGrail, B. P.; Schaef, H. T.; Glezakou, V.-A.; Dang, L. X.; Owen, A. T. Water reactivity
1651 in the liquid and supercritical CO_2 phase: Has half the story been neglected? *Energy*
1652 *Procedia* **2009**, *1*, 3415–3419.

1653 (367) Kwak, J. H.; Hu, J. Z.; Turcu, R. V. F.; Rosso, K. M.; Ilton, E. S.; Wang, C.; Sears, J. A.;
1654 Engelhard, M. H.; Felmy, A. R.; Hoyt, D. W. The role of H_2O in the carbonation of
1655 forsterite in supercritical CO_2. *Int. J. Greenh. Gas Control* **2011**, *5*, 1081–1092.

1656 (368) Regnault, O.; Lagneau, V.; Catalette, H.; Schneider, H. Experimental study of pure
1657 mineral phases/supercritical CO_2 reactivity. Implications for geological CO_2 sequestration.
1658 *Comptes Rendus Geosci.* **2005**, *337*, 1331–1339.

1659 (369) Thompson, C. J.; Loring, J. S.; Rosso, K. M.; Wang, Z. Comparative reactivity study of
1660 forsterite and antigorite in wet supercritical CO_2 by in situ infrared spectroscopy. *Int. J.*
1661 *Greenh. Gas Control* **2013**, *18*, 246–255.

1662 (370) Wang, X.; Alvarado, V.; Swoboda-Colberg, N.; Kaszuba, J. P. Reactivity of dolomite in
1663 water-saturated supercritical carbon dioxide: Significance for carbon capture and storage
1664 and for enhanced oil and gas recovery. *Energy Convers. Manag.* **2013**, *65*, 564–573.

1665   (371) Qafoku, O.; Hu, J.; Hess, N. J.; Hu, M. Y.; Ilton, E. S.; Feng, J.; Arey, B. W.; Felmy, A.
1666   R. Formation of submicron magnesite during reaction of natural forsterite in H_2O-
1667   saturated supercritical CO_2. *Geochim. Cosmochim. Acta* **2014**, *134*, 197–209.

1668   (372) Trémosa, J.; Castillo, C.; Vong, C. Q.; Kervévan, C.; Lassin, A.; Audigane, P. Long-term
1669   assessment of geochemical reactivity of CO_2 storage in highly saline aquifers: Application
1670   to Ketzin, In Salah and Snøhvit storage sites. *Int. J. Greenh. Gas Control* **2014**, *20*, 2–26.

1671   (373) Hedlund, T.; Sjöberg, S.; Öhman, L.-O. Equilibrium and structural studies of silicon(IV)
1672   and aluminium(III) in aqueous solution. 15. A potentiometric study of speciation and
1673   equilibria in the Al^{3+}-CO_2(g)-OH^- system. *Acta Chem. Scand. A* **1987**, *41*, 197–207.

1674   (374) Brunauer, S.; Emmett, P. H.; Teller, E. Adsorption of gases in multimolecular layers. *J.*
1675   *Am. Chem. Soc.* **1938**, *60*, 309–319.

1676   (375) Gunter, W. D.; Perkins, E. H.; Hutcheon, I. Aquifer disposal of acid gases: modelling of
1677   water–rock reactions for trapping of acid wastes. *Appl. Geochemistry* **2000**, *15*, 1085–
1678   1095.

1679   (376) White, S. P.; Allis, R. G.; Moore, J.; Chidsey, T.; Morgan, C.; Gwynn, W.; Adams, M.
1680   Simulation of reactive transport of injected CO_2 on the Colorado Plateau, Utah, USA.
1681   *Chem. Geol.* **2005**, *217*, 387–405.

1682   (377) Xu, T.; Apps, J. A.; Pruess, K. Mineral sequestration of carbon dioxide in a sandstone–
1683   shale system. *Chem. Geol.* **2005**, *217*, 295–318.

1684   (378) Zerai, B.; Saylor, B. Z.; Matisoff, G. Computer simulation of CO_2 trapped through mineral
1685   precipitation in the Rose Run Sandstone, Ohio. *Appl. Geochemistry* **2006**, *21*, 223–240.

1686   (379) Zhang, W.; Li, Y.; Xu, T.; Cheng, H.; Zheng, Y.; Xiong, P. Long-term variations of CO_2
1687   trapped in different mechanisms in deep saline formations: A case study of the Songliao
1688   Basin, China. *Int. J. Greenh. Gas Control* **2009**, *3*, 161–180.

1689   (380) Xu, T.; Yue, G.; Wang, F.; Liu, N. Using natural CO_2 reservoir to constrain geochemical
1690   models for CO_2 geological sequestration. *Appl. Geochemistry* **2014**, *43*, 22–34.

1691   (381) Peters, C. A. Accessibilities of reactive minerals in consolidated sedimentary rock: An
1692   imaging study of three sandstones. *Chem. Geol.* **2009**, *265*, 198–208.

1693   (382) White, A. F.; Peterson, M. L. Role of reactive-surface-area characterization in
1694   geochemical kinetic Models. *ACS Symp. Ser.* **1990**, *416*, 461–475.

1695   (383) Beni, A. N.; Stanjek, H.; Clauser, C. The formation of iron hydroxide coatings in an
1696   Emscher Marl: inverse reactive transport modeling of reactive surface area. *Environ.*
1697   *Earth Sci.* **2014**, *71*, 763–771.

1698   (384)   Xu, T.; Pruess, K. Modeling multiphase non-isothermal fluid flow and reactive
1699   geochemical transport in variably saturated fractured rocks: 1. Methodology. *Am. J. Sci.*
1700   **2001**, *301*, 16–33.

1701   (385)   Johnson, J. W.; Nitao, J. J.; Knauss, K. G. Reactive transport modelling of CO_2 storage in
1702   saline aquifers to elucidate fundamental processes, trapping mechanisms, and
1703   sequestration partitioning. In *Geological Storage of Carbon Dioxide, Geological Society*
1704   *of London Special Publication 233*; Bains, S. J., Worden, R. H., Eds.; Geological Society,
1705   London, 2004.

1706   (386)   Audigane, P.; Gaus, I.; Pruess, K.; Xu, T. Reactive transport modeling using
1707   TOUGHREACT for the long term CO_2 storage at Sleipner, North Sea. In *Proceedings of*
1708   *the 4th Annual Conference on Carbon Capture and Sequestration DOE/NETL*; 2005; Vol.
1709   2.

1710   (387)   Knauss, K. G.; Johnson, J. W.; Steefel, C. I. Evaluation of the impact of CO_2, co-
1711   contaminant gas, aqueous fluid and reservoir rock interactions on the geologic
1712   sequestration of CO_2. *Chem. Geol.* **2005**, *217*, 339–350.

1713   (388)   Ozah, R. C.; Lakshminarasimhan, S.; Pope, G. A.; Sepehrnoori, K.; Bryant, S. L.
1714   Numerical simulation of the storage of pure CO_2 and CO_2-H_2S gas mixtures in deep saline
1715   aquifers. In *2005 SPE Annual Technical Conference and Exhibition, Dallas, TX, 9-12*
1716   *October 2005*; SPE Paper 97255, Society of Petroleum Engineers, 2005.

1717   (389)   Balashov, V. N.; Guthrie, G. D.; Hakala, J. A.; Lopano, C. L.; Rimstidt, J. D.; Brantley, S.
1718   L. Predictive modeling of CO_2 sequestration in deep saline sandstone reservoirs: Impacts
1719   of geochemical kinetics. *Appl. Geochemistry* **2013**, *30*, 41–56.

1720   (390)   Bolourinejad, P.; Omrani, P. S.; Herber, R. Effect of reactive surface area of minerals on
1721   mineralization and carbon dioxide trapping in a depleted gas reservoir. *Int. J. Greenh. Gas*
1722   *Control* **2014**, *21*, 11–22.

1723   (391)   Luhmann, A. J.; Kong, X.-Z.; Tutolo, B. M.; Garapati, N.; Bagley, B. C.; Saar, M. O.;
1724   Seyfried, W. E., Jr. Experimental dissolution of dolomite by CO_2-charged brine at 100 °C
1725   and 150 bar: Evolution of porosity, permeability, and reactive surface area. *Chem. Geol.*
1726   **2014**, *380*, 145–160.

1727   (392)   Li, L.; Peters, C. A.; Celia, M. A. Upscaling geochemical reaction rates using pore-scale
1728   network modeling. *Adv. Water Resour.* **2006**, *29*, 1351–1370.

1729   (393)   Molins, S.; Trebotich, D.; Yang, L.; Ajo-Franklin, J. B.; Ligocki, T. J.; Shen, C.; Steefel,
1730   C. I. Pore-scale controls on calcite dissolution rates from flow-through laboratory and
1731   numerical experiments. *Environ. Sci. Technol.* **2014**, *48*, 7453–7460.

1732   (394)   Fischer, C.; Arvidson, R. S.; Lüttge, A. How predictable are dissolution rates of crystalline
1733   material? *Geochim. Cosmochim. Acta* **2012**, *98*, 177–185.

1734　(395) Landrot, G.; Ajo-Franklin, J. B.; Yang, L.; Cabrini, S.; Steefel, C. I. Measurement of
1735　　　　accessible reactive surface area in a sandstone, with application to CO_2 mineralization.
1736　　　　*Chem. Geol.* **2012**, *318-319*, 113–125.

1737　(396) Skovbjerg, L. L.; Hassenkam, T.; Makovicky, E.; Hem, C. P.; Yang, M.; Bovet, N.; Stipp,
1738　　　　S. L. S. Nano sized clay detected on chalk particle surfaces. *Geochim. Cosmochim. Acta*
1739　　　　**2012**, *99*, 57–70.

1740　(397) Andreani, M.; Luquot, L.; Gouze, P.; Godard, M.; Hoisé, E.; Gibert, B. Experimental
1741　　　　study of carbon sequestration reactions controlled by the percolation of CO_2-rich brine
1742　　　　through peridotites. *Environ. Sci. Technol.* **2009**, *43*, 1226–1231.

1743　(398) Daval, D.; Sissmann, O.; Menguy, N.; Saldi, G. D.; Guyot, F.; Martinez, I.; Corvisier, J.;
1744　　　　Garcia, B.; Machouk, I.; Knauss, K. G.; et al. Influence of amorphous silica layer
1745　　　　formation on the dissolution rate of olivine at 90°C and elevated pCO_2. *Chem. Geol.* **2011**,
1746　　　　*284*, 193–209.

1747　(399) Gin, S.; Guittonneau, C.; Godon, N.; Neff, D.; Rebiscoul, D.; Cabié, M.; Mostefaoui, S.
1748　　　　Nuclear glass durability: New insight into alteration layer properties. *J. Phys. Chem. C*
1749　　　　**2011**, *115*, 18696–18706.

1750　(400) Béarat, H.; McKelvy, M. J.; Chizmeshya, A. V. G.; Gormley, D.; Nunez, R.; Carpenter, R.
1751　　　　W.; Squires, K.; Wolf, G. H. Carbon sequestration via aqueous olivine mineral
1752　　　　carbonation: Role of passivating layer formation. *Environ. Sci. Technol.* **2006**, *40*, 4802–
1753　　　　4808.

1754　(401) Zhu, C.; Veblen, D. R.; Blum, A. E.; Chipera, S. J. Naturally weathered feldspar surfaces
1755　　　　in the Navajo Sandstone aquifer, Black Mesa, Arizona: Electron microscopic
1756　　　　characterization. *Geochim. Cosmochim. Acta* **2006**, *70*, 4600–4616.

1757　(402) Stockmann, G. J.; Wolff-Boenisch, D.; Gislason, S. R.; Oelkers, E. H. Do carbonate
1758　　　　precipitates affect dissolution kinetics?: 2: Diopside. *Chem. Geol.* **2013**, *337-338*, 56–66.

1759　(403) Stockmann, G. J.; Wolff-Boenisch, D.; Bovet, N.; Gislason, S. R.; Oelkers, E. H. The role
1760　　　　of silicate surfaces on calcite precipitation kinetics. *Geochim. Cosmochim. Acta* **2014**,
1761　　　　*135*, 231–250.

1762　(404) Stockmann, G. J.; Wolff-Boenisch, D.; Gislason, S. R.; Oelkers, E. H. Do carbonate
1763　　　　precipitates affect dissolution kinetics? 1: Basaltic glass. *Chem. Geol.* **2011**, *284*, 306–
1764　　　　316.

1765　(405) Emmanuel, S. Mechanisms influencing micron and nanometer-scale reaction rate patterns
1766　　　　during dolostone dissolution. *Chem. Geol.* **2014**, *363*, 262–269.

1767   (406) Cubillas, P.; Köhler, S.; Prieto, M.; Causserand, C.; Oelkers, E. H. How do mineral
1768   coatings affect dissolution rates? An experimental study of coupled $CaCO_3$ dissolution—
1769 $CdCO_3$ precipitation. *Geochim. Cosmochim. Acta* **2005**, *69*, 5459–5476.

1770   (407) Daval, D.; Hellmann, R.; Saldi, G. D.; Wirth, R.; Knauss, K. G. Linking nm-scale
1771   measurements of the anisotropy of silicate surface reactivity to macroscopic dissolution
1772   rate laws: New insights based on diopside. *Geochim. Cosmochim. Acta* **2013**, *107*, 121–
1773   134.

1774   (408) Sissmann, O.; Brunet, F.; Martinez, I.; Guyot, F.; Verlaguet, A.; Pinquier, Y.; Daval, D.
1775   Enhanced olivine carbonation within a basalt as compared to single-phase experiments:
1776   Reevaluating the potential of CO_2 mineral sequestration. *Environ. Sci. Technol.* **2014**, *48*,
1777   5512–5519.

1778   (409) Hellmann, R.; Wirth, R.; Daval, D.; Barnes, J.-P.; Penisson, J.-M.; Tisserand, D.; Epicier,
1779   T.; Florin, B.; Hervig, R. L. Unifying natural and laboratory chemical weathering with
1780   interfacial dissolution–reprecipitation: A study based on the nanometer-scale chemistry of
1781   fluid–silicate interfaces. *Chem. Geol.* **2012**, *294-295*, 203–216.

1782   (410) Zhu, C.; Lu, P. The coupling of dissolution and precipitation reactions as the main
1783   contributor to the apparent field-lab rate discrepancy. *Procedia Earth Planet. Sci.* **2013**, *7*,
1784   948–952.

1785   (411) Hellmann, R.; Penisson, J.-M.; Hervig, R. L.; Thomassin, J.-H.; Abrioux, M.-F. An
1786   EFTEM/HRTEM high-resolution study of the near surface of labradorite feldspar altered
1787   at acid pH: evidence for interfacial dissolution-reprecipitation. *Phys. Chem. Miner.* **2003**,
1788   *30*, 192–197.

1789   (412) Amrhein, C.; Suarez, D. L. Some factors affecting the dissolution kinetics of anorthite at
1790   25°C. *Geochim. Cosmochim. Acta* **1992**, *56*, 1815–1826.

1791   (413) Urosevic, M.; Rodriguez-Navarro, C.; Putnis, C. V.; Cardell, C.; Putnis, A.; Ruiz-Agudo,
1792   E. In situ nanoscale observations of the dissolution of {1014} dolomite cleavage surfaces.
1793   *Geochim. Cosmochim. Acta* **2012**, *80*, 1–13.

1794   (414) Schott, J.; Pokrovsky, O. S.; Spalla, O.; Devreux, F.; Gloter, A.; Mielczarski, J. A.
1795   Formation, growth and transformation of leached layers during silicate minerals
1796   dissolution: The example of wollastonite. *Geochim. Cosmochim. Acta* **2012**, *98*, 259–281.

1797   (415) Gin, S.; Jollivet, P.; Fournier, M.; Angeli, F.; Frugier, P.; Charpentier, T. Origin and
1798   consequences of silicate glass passivation by surface layers. *Nat. Commun.* **2015**, *6*, 6360.

1799   (416) Moore, J.; Lichtner, P. C.; White, A. F.; Brantley, S. L. Using a reactive transport model
1800   to elucidate differences between laboratory and field dissolution rates in regolith.
1801   *Geochim. Cosmochim. Acta* **2012**, *93*, 235–261.

1802

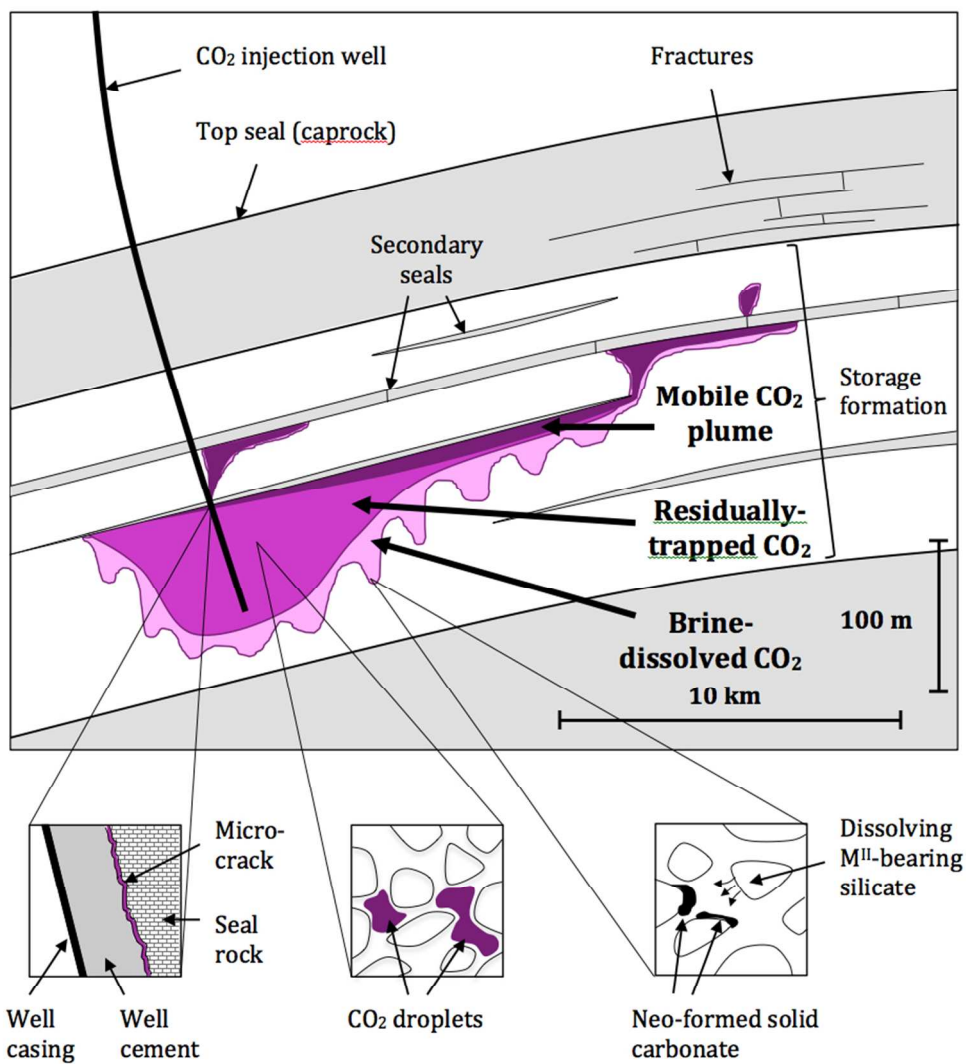1803   Table of Contents Graphic.
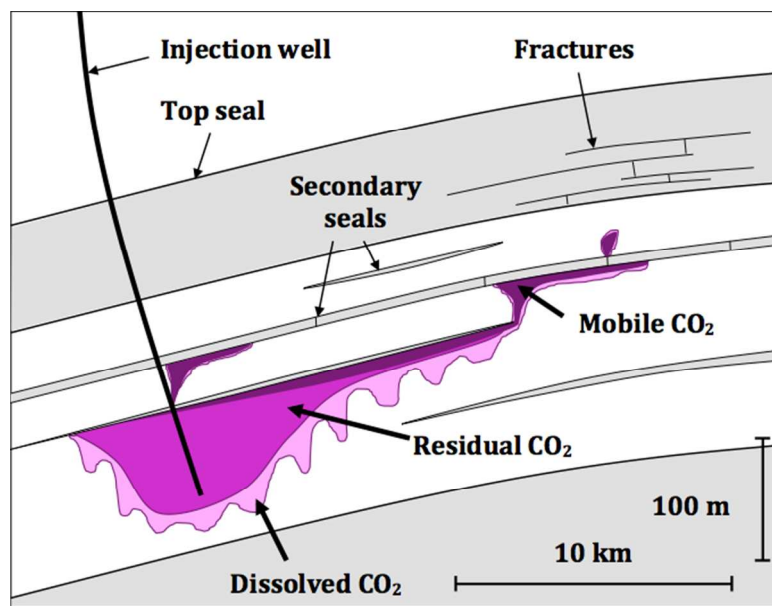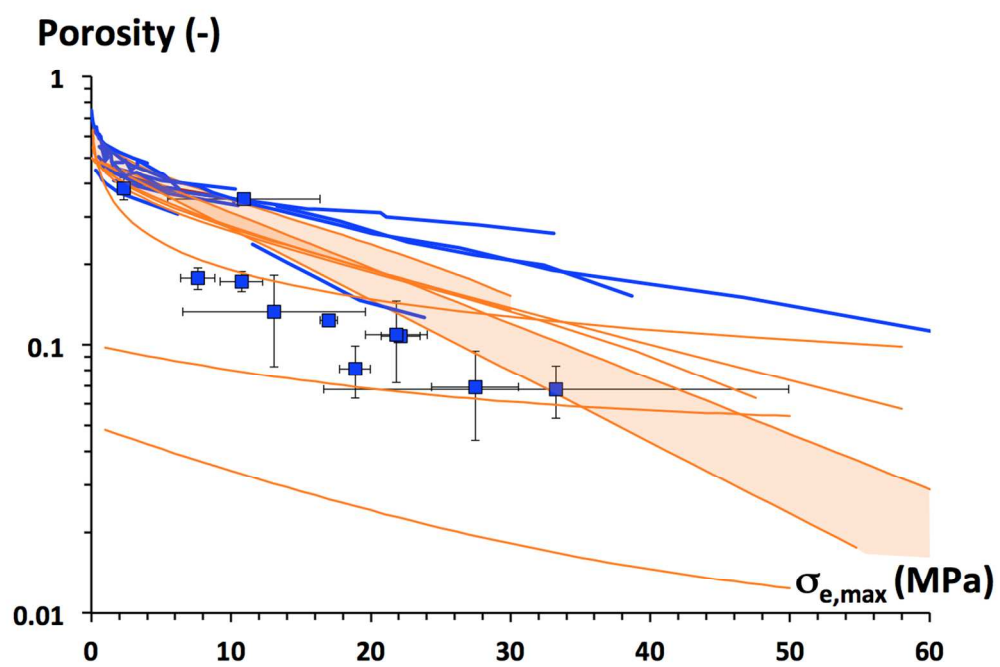
1804

1805

Figure 1
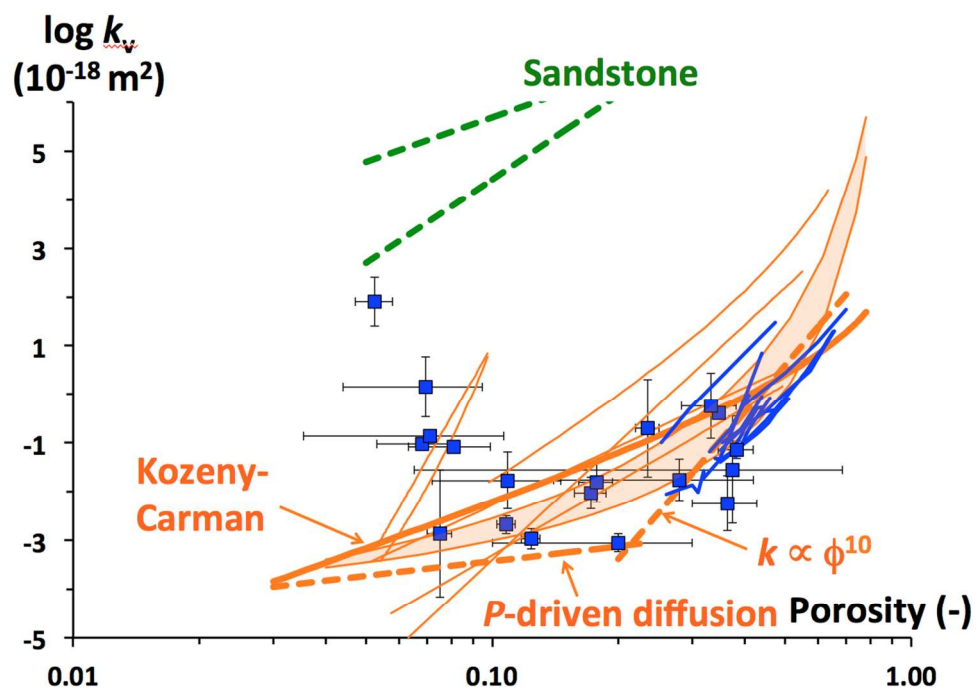80x88mm (300 x 300 DPI)

Figure 2a
117x83mm (300 x 300 DPI)

Figure 2b
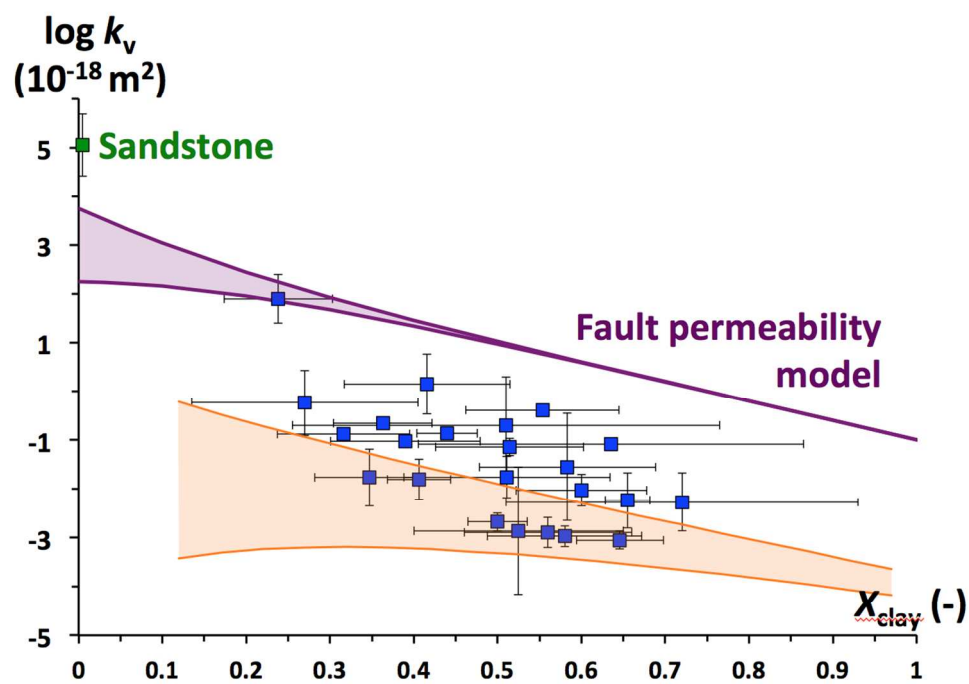118x83mm (300 x 300 DPI)
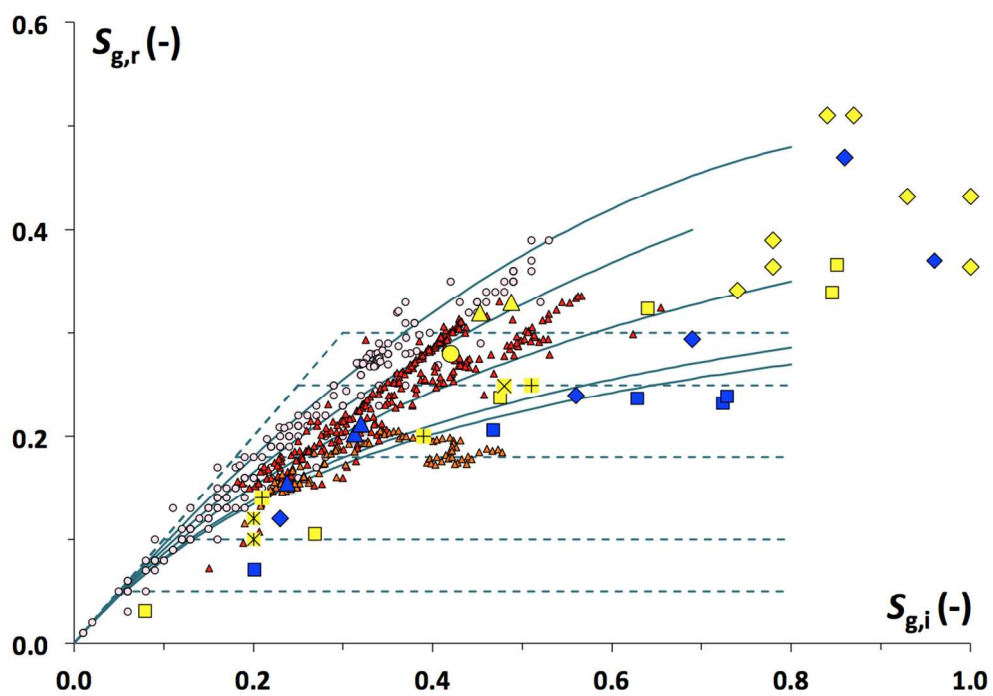
Figure 2c
117x83mm (300 x 300 DPI)
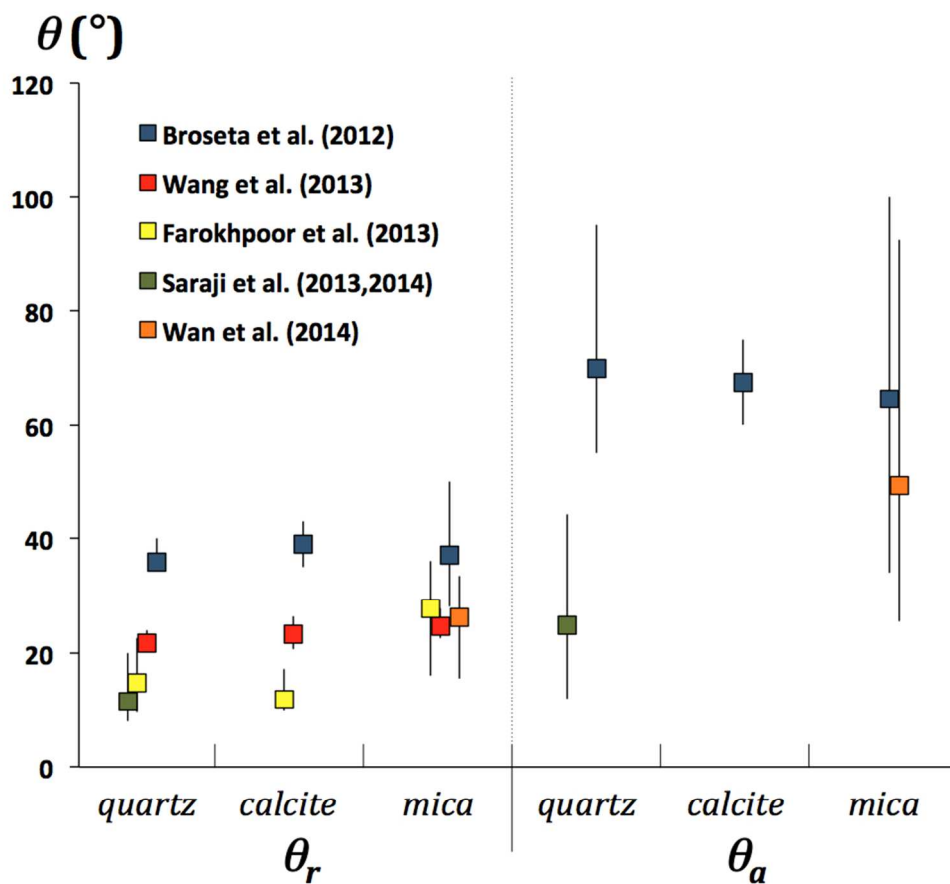
Figure 3
121x85mm (300 x 300 DPI)
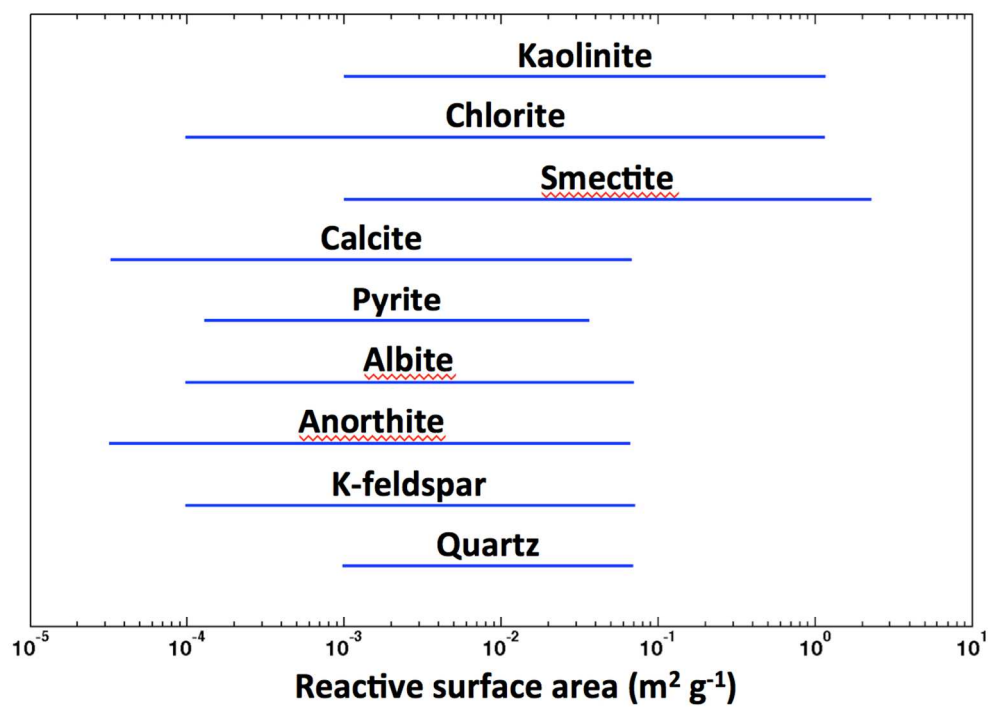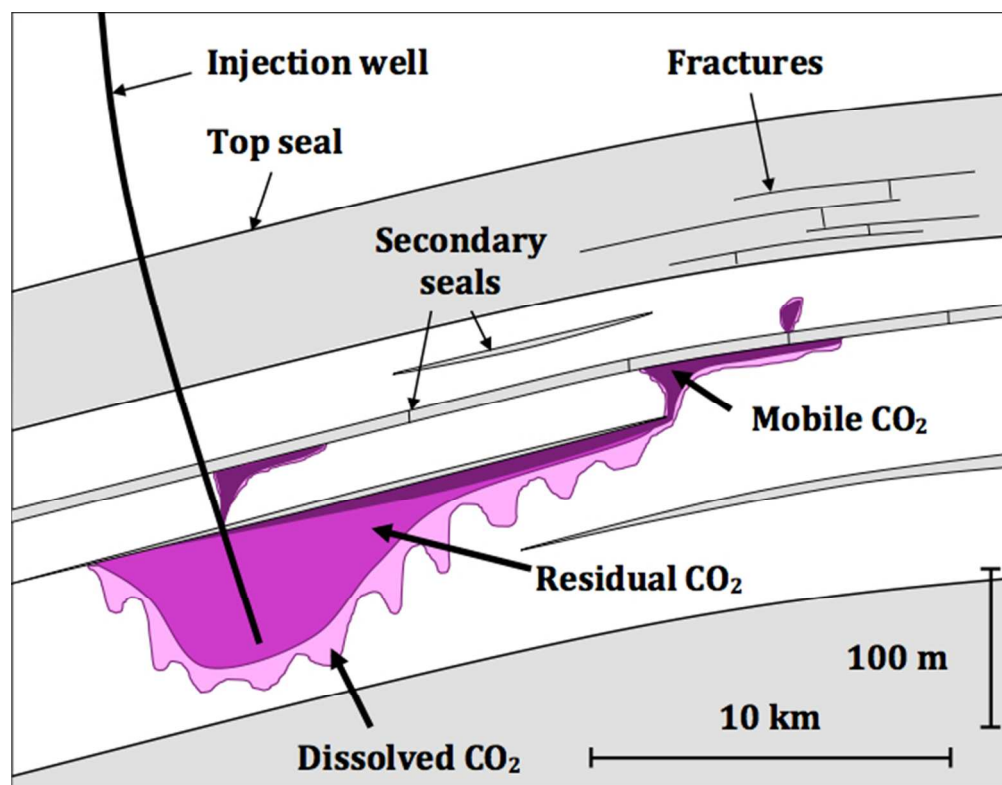
Figure 4
85x77mm (300 x 300 DPI)

Figure 5
111x80mm (300 x 300 DPI)

TOC Art
57x44mm (300 x 300 DPI)